CCR7^{+} DC Define a Type 17 Module in Psoriasis

Yang SUN[1,6], Fangzhou LOU[1,6], Xiaojie CAI[1], Zhikai WANG[1], Xiuli YANG[1], Libo SUN[1], Zhouwei WU[2], Zhaoyuan LIU[3], Yu-Ling SHI[4], Florent GINHOUX[1,3,5], and Honglin WANG[1,*]

[1]Precision Research Center for Refractory Diseases, Shanghai General Hospital, Shanghai Jiao Tong University School of Medicine, Shanghai 201620, China

[2]Department of Dermatology, Shanghai General Hospital, Shanghai Jiao Tong University School of Medicine, Shanghai 200080, China

[3]Shanghai Institute of Immunology, Shanghai Jiao Tong University School of Medicine, Shanghai 200025, China

[4]Department of Dermatology, Shanghai Skin Disease Hospital, Tongji University School of Medicine, Shanghai 200443, China

[5]Institut Gustave Roussy, Villejuif 94805, France

[6]These authors contributed equally.

[*]Correspondence to:

Honglin WANG, Ph.D.
Precision Research Center for Refractory Diseases, Shanghai General Hospital, Shanghai Jiao Tong University School of Medicine, Shanghai 201620, China
E-mail: honglin.wang@sjtu.edu.cn

HIGHLIGHTS

- *IL4I1*$^{+}$*CD200*$^{+}$*CCR7*$^{+}$ DC are dominant IL-23 producers in psoriasis and its mouse model.
- Psoriatic CCR7^{+} DC likely arise from cDC2.
- CD161 marks all IL-17-producing T cells in psoriatic skin.
- IL-23a overexpression in CCR7^{+} DC elicits an αβT cell-driven mouse model of psoriasis and arthritis.
- CCR7^{+} DC spatially define a type 17 module in psoriatic epidermis.

ABSTRACT

Interleukin (IL)-23 is the master pathogenic cytokine in psoriasis and neutralization of IL-23 alleviates psoriasis. Psoriasis relapses after the withdrawal of IL-23 antibodies, and the persistence of IL-23-producing cells probably contributes to such recurrence. However, the cellular source of IL-23 was unclear, which hinders the development of targeted therapies focusing on modulating IL-23 expression aimed at resolving relapse. Here, we showed that *IL4I1*$^{+}$*CD200*$^{+}$*CCR7*$^{+}$ dendritic cells (CCR7^{+} DC) dominantly produced IL-23 by concomitantly expressing the IL-23A and IL-12B subunits in human psoriatic skin. Deletion of CCR7^{+} DC completely abrogated IL-23 production in a mouse model of psoriasis and enforced expression of IL-23a in CCR7^{+} DC elicited not only αβT cell-driven psoriasis-like skin disease, but also arthritis. CCR7^{+} DC co-localized with CD161^{+} IL-17-producing T cells and KRT17^{+} keratinocytes, which were located in the outermost layers of psoriatic epidermis and strongly exhibited IL-17 downstream signatures. Based on these data, we identified CCR7^{+} DC as the source of IL-23 in psoriasis, which paves the way for the design of therapies focused on manipulating IL-23 production that may resolve the relapse of chronic inflammatory disorders like psoriasis.

INTRODUCTION

Psoriasis is a chronic and recurrent immune-mediated skin disorder affecting 125 million people globally(Armstrong and Read, 2020). It manifests as erythematous skin plaques covered with white scales, which impact the quality of life of patients both physically and psychologically(Griffiths and Barker, 2007). Although neutralization of pro-inflammatory cytokines, including IL-17A and IL-23, alleviates psoriasis symptoms, many patients are unresponsive or respond only partially to such therapies. In addition, responsive patients face the risk of drug resistance, or recurrence following the discontinuation of biologic agents(Amschler et al., 2020; Bito et al., 2014; Galluzzo et al., 2018; Masson Regnault et al., 2022), the latter being a key challenge in psoriasis therapy(Puig et al., 2022).

Interleukin (IL)-17-producing $CD4^+$ T helper 17 (Th17) cells were initially identified as crucial players in psoriasis-associated-immune circuits. Later, $CD8^+$ T cells were found to contain the T cytotoxic 17 (Tc17) population, giving rise to *in situ* IL-17 production(Kryczek et al., 2008; Lowes et al., 2008; Ortega et al., 2009). Recent studies revealed key roles of $CD8^+$ tissue-resident memory T (T_{RM}) cells in the epidermis as sources of IL-17 in inflamed psoriatic skin, and as rapid responders in recall responses in resolved psoriasis(Cheuk et al., 2017; Cheuk et al., 2014). These T_{RM} cells are considered to be the immediate cause of the relapse of psoriasis(Conrad et al., 2007). While IL-17 is produced mainly by αβT cells in human psoriatic skin, psoriasis-like mouse models are mostly driven by γδT cell-derived IL-17(Cai et al., 2011; Mabuchi et al., 2011). This reflects distinct differences in the immunopathological principles in human psoriasis versus mouse models, which hinders the effective evaluation of drug candidates aimed at preventing psoriasis recurrence.

As subpopulations of the dendritic cell (DC) population, both plasmacytoid DCs (pDC) and conventional DCs (cDC), are considered drivers of psoriasis. The type 1 IFN-producing pDC are crucial for the initiation of psoriasis(Nestle et al., 2005), while the cDC secrete IL-23 as a third signal that induces polarization toward a type 17 T cell response in the disease(Wohn et al., 2013). Specific targeting of IL-23 in psoriasis has

been demonstrated to effectively prolong the time to relapse, which further emphasizes the key role of IL-23 in the recurrence and maintenance of psoriasis, and highlights manipulation of IL-23 production as a potential therapeutic strategy(Masson Regnault et al., 2022). Although IL-23 in psoriasis-like mouse skin is reported to be produced by CD301b$^+$ cDC2, the counterpart of these DCs in human skin as well as the exact cellular source of IL-23 in psoriasis remain elusive(Guttman-Yassky et al., 2011; Hansel et al., 2011; Kim et al., 2018; Nakamizo et al., 2021; Whitley et al., 2022). Thus, identification of the IL-23 producers in psoriasis is a critical step for developing novel therapeutic strategies aimed at resolving relapse.

Here, we showed that *IL4I1*$^+$*CD200*$^+$*CCR7*$^+$ DC (CCR7$^+$ DC), but not other myeloid cells, produced IL-23 by concomitantly expressing the IL-23A and IL-12B subunits, both of which are required to form the intact IL-23 for extracellular secretion, in psoriasis. Furthermore, we identified CCR7$^+$ DC as the major source of IL-23 in the skin in the imiquimod (IMQ)-induced psoriasis-like mouse model. Importantly, Il4i1$^+$ cell-specific overexpression of IL-23a elicited an αβT cell-driven psoriasis-like mouse model, which also developed psoriatic arthritis-like symptoms, with lesions that transcriptionally mimicked human psoriasis. In human psoriatic skin, IL-23-producing CCR7$^+$ DC localized spatially with IL-17-producing CD161$^+$ T cells and the IL-17-responsive KRT17$^+$ keratinocyte subpopulation, defining a type 17 module that can be harnessed for the discovery of drug targets and rational design of therapeutic strategies for psoriasis.

RESULTS

Psoriatic keratinocytes exhibit a reconstructed differentiation trajectory

To identify immune and non-immune cells that might be involved in the development of psoriasis, we generated transcriptomes of individual epidermis and dermis cells obtained from six psoriasis patients and four healthy donors using the 10× Genomics platform (**Figures S1A** and **S1B**). After the epidermis was dissociated from the dermis by enzymatic digestion, live epidermal cells and live $CD45^+$ dermal leukocytes were sorted from each sample using fluorescence activated cell sorting (FACS) and subjected to 3'-barcoded scRNA-seq to generate unique molecular identifier (UMI) counts matrixes (**Figures S1C** and **S1D**). After quality control and doublet exclusion, 31,750 epidermal cells and 42,054 dermal leukocytes from the 20 samples were integrated and clustered jointly. We performed uniform manifold approximation and projection (UMAP) dimensional reduction and partitioned the cells according to their respective marker genes (**Figures S1D** and **S1E**)(Becht et al., 2018). We identified keratinocytes, T cells, myeloid cells, mast cells, pDC and B cells in our data (**Figures S1D** and **S1E**).

To characterize non-immune cells in psoriatic epidermis, we extracted keratinocytes from the integrated data of all 10 epidermal samples for UMAP dimensional reduction and named the sub-clusters according to their hallmark genes (**Figures S2A** and **S2B**). Comparison of the interfollicular keratinocyte sub-clusters of psoriatic epidermis to those of healthy epidermis showed that: (1) *KRT14* and *KRT5* were highly upregulated not only in basal keratinocyte sub-clusters ($KRT14^+$_$ASS1^+$ and $KRT14^+$_$KRT15^{hi}$), but also in suprabasal keratinocyte sub-clusters of psoriatic epidermis; (2) spinous keratinocytes ($KRT10^+$_$KRT5^{hi}$ and $KRT10^+$_$KRT2^+$) normally express *KRT10*, *KRT1* and *KRT2*, while these genes were downregulated in psoriatic lesions; (3) Expression of *KRT6*, *KRT16* and *KRT17*, which were shown to be induced by T cell-derived cytokines

including IFN-γ, IL-17 and IL-22(Yang et al., 2017; Zhang et al., 2019), was higher in psoriatic keratinocytes than in normal controls, with upregulated *KRT17* specifically detected in *KRT17*$^+$ keratinocytes (KRT17$^+$) and granular keratinocytes (FLG$^+$) of psoriatic epidermis; and (4) psoriatic keratinocytes upregulated IL-17A-downstream genes including *S100A8*, *S100A9*, *SERPINB3* and *SERPINB4*, and IFN-γ-downstream genes including *ISG15*, *IFITM1*, *IFI6*, *IFITM3* and *IFI27*, in comparison to healthy keratinocytes (**Figures S2B** and **S2C**). Employing a pseudo-time trajectory to potentially understand the differentiation programs of healthy and psoriatic keratinocytes, we found a delayed decline in *KRT14* expression, abnormal upregulation of *MKI67* and *KRT17* in the end of the pseudo-time line, and the absence of the terminal differentiation marker *LOR* in psoriatic interfollicular keratinocytes (**Figure S2D**). These data highlighted dysregulated keratinocyte differentiation and proliferation in the different layers of psoriatic epidermis, a process that is probably regulated by diverse inflammatory cues from T cells.

KRT17$^+$ keratinocytes respond to IL-17 derived from CD161$^+$ T cells

To gain functional insights into the T cells driving such aberrant keratinocyte differentiation, we investigated the T cell heterogeneity in psoriatic skin in comparison to normal skin. *CD3*$^+$ T cells were extracted from the integrated data, and further sub-clustered (**Figures 1A** and **1B**). *KLRB1*$^+$ (CD161$^+$) T cells (KLRB1_T) and *CD8*$^+$ T cells (CD8_Cytotoxic_T and CD8_T_{RM}) expressed high levels of T_{RM} cell markers including *CD69* and *ITGAE*, while *CD4*$^+$*FOXP3*$^+$ T_{reg} cells expressed *CCR7*, but not T_{RM} cell markers (**Figure S3A**). Importantly, *IL17A*, *IL17F* and *IL26* expression was almost completely confined to "KLRB1_T" cells (**Figure 1B**), which were characterized as *KLRB1*$^+$ αβT cells as these cells expressed *TRAC*, but not *TRDC* (**Figure S3A**). Notably, increased percentages of *IL17A*$^+$ T cells, *IL17F*$^+$ T cells and *IL26*$^+$ T cells were identified among the *KLRB1*$^+$ αβT cells of psoriatic skin compared to normal skin (**Figure 1C**).

Given that $CD4^+$ Th17 cells and $CD8^+$ Tc17 cells were reported to produce IL-17 in psoriasis(Ho and Kupper, 2019), we calculated the ratios of *CD4*$^+$, *CD8*$^+$, *CD4*$^+$*CD8*$^+$ and *CD4*$^-$*CD8*$^-$ among the *KLRB1*$^+$ αβT cells. The *KLRB1*$^+$ αβT cell population consisted of approximately 20% *CD4*$^+$ T cells, 20% *CD8*$^+$ T cells and 60% *CD4*$^-$*CD8*$^-$ T cells, and these percentages did not differ between normal and psoriatic skin samples (**Figure S3B**). Notably, a significantly higher proportion of the *CD4*$^-$*CD8*$^-$ T cells expressing *IL17A* among the *KLRB1*$^+$ αβT cell population was found in psoriatic skin compared to normal skin (**Figure 1D**).

IL-17A induces changes in the expression of psoriasis-associated gene sets in keratinocytes(Muromoto et al., 2016). To dissect the reactivity of keratinocytes to IL-17A, we aggregated the interfollicular keratinocyte sub-clusters as basal (KRT14$^+$_ASS1$^+$ and KRT14$^+$_KRT15^{hi}), spinous (KRT10$^+$_KRT5^{hi} and KRT10$^+$_KRT2$^+$), mitotic (PTTG1^{hi} and PCNA^{hi}) and KRT17 (KRT17$^+$). We then compared these keratinocyte sub-populations using an IL-17A-downstream signature gene set(Muromoto et al., 2016). KRT17 showed enrichment in IL-17A signaling compared to basal, mitotic, and spinous keratinocytes **(Figure 1E)**. We also performed spatial transcriptomic analysis on psoriatic skin sections to visualize genes involved in IL-17 responses (**Figure S1A**). In accordance with the gene set enrichment analysis (GSEA), spatial plotting of the IL-17A-downstream signatures showed that *SERPINB4* and *DEFB4A* co-localized with *KRT17* in the outermost layers of psoriatic epidermis **(Figures 1F** and **S4A)**. However, neither spatial plotting nor immunofluorescence staining showed any preferential co-localization of IL17RA with KRT17$^+$ keratinocytes **(Figures S4A-S4C)**. We hypothesized that in addition to expressing IL17RA, KRT17$^+$ keratinocyte induction also required additional IL-17. Importantly, we found that *IL17A*$^+$ or *IL17F*$^+$ spots were intimately co-localized with KRT17$^+$ keratinocytes in psoriatic skin (**Figures 1G** and **S5**). *In situ* RNA hybridization of *IL17A* combined with immunofluorescence staining of KRT17 further

confirmed the proximity of IL-17-producing T cells with KRT17$^+$ keratinocytes (**Figure 1H**). Together, our data suggested that CD161$^+$ αβT cell-derived IL-17 acts on adjacent KRT17$^+$ keratinocytes to promote and maintain auto-inflammation in psoriasis.

CCR7$^+$ DC are major IL-23 producers in psoriasis

Human DCs and monocytes are highly heterogeneous in their origins and functions(Anderson et al., 2021; Dress et al., 2020), and their contributions to psoriasis pathophysiology remain to be elucidated, although cDC secrete IL-23 as a third signal that induces polarization toward a type 17 T cell response that drives psoriatic plaque formation in mice(Wohn et al., 2013). Based on our transcriptomic analysis, we detected cDC1 (*CLEC9A*$^+$*IRF8*$^+$), cDC2 (*CLEC10A*$^+$*CD1C*$^+$), DC3 (*CD14*$^+$*CD1C*$^+$)(Nakamizo et al., 2021), monocytes/macrophages (*CD14*$^+$*C1QA*$^+$), CCR7$^+$ DC (*CCR7*$^+$*LAMP3*$^+$*CD200*$^+$*IL4I1*$^+$)(Maier et al., 2020), LC (*CD1A*$^+$*CD207*$^+$), pDC (*JCHAIN*$^+$*IRF7*$^+$) and AXL$^+$ DC (*AXL*$^+$)(See et al., 2017) in psoriatic and healthy skin (**Figures 2A** and **S6A**).

Gene expression analysis of DCs and monocytes in psoriatic skin revealed that CCR7$^+$ DC expressed high levels of HLA genes, including *CD1B*, *CD1E*, *HLA-A*, *HLA-B*, and *HLA-C*, and T cell co-stimulatory or co-inhibitory genes, including *CD40*, *CD80*, *CD86*, *CD200*, *CD274*, *CD70* and *PDCD1LG2* (**Figure 2B**). These findings indicated that CCR7$^+$ DC express all the key molecules required to activate T cells in psoriatic skin. Moreover, *IL12B* (encoding IL-12p40) and *IL23A* (encoding IL-23p19), which form the intact IL-23 for extracellular secretion(Oppmann et al., 2000), were expressed at high levels by CCR7$^+$ DC, but not other types of DCs or monocytes, suggesting that CCR7$^+$ DC are potent IL-23-producers and type 17 T cell response-inducers (**Figure 2C**). Single-molecule *in situ* RNA hybridization of *IL23A* and *IL12B* as well as the CCR7$^+$ DC marker *CD200* in human psoriatic skin sections revealed a small fraction of *CD200*$^+$ cells

expressing both *IL23A* and *IL12B* (**Figure 2D**). Flow cytometric analysis of psoriatic skin showed that CD11C$^+$ pan DC consisted of IL-12p40$^-$IL-23p19$^-$, IL-12p40$^-$IL-23p19$^+$, and IL-12p40$^+$IL-23p19$^+$ populations (**Figures S6B** and **S6C**), with the IL-12p40$^+$IL-23p19$^+$ cells confined to the CD1B$^+$CD200$^+$CCR7$^+$ DC population (**Figures S6B** and **2E**). Given that IL-23p19 shows no biological activity without forming a heterodimer with IL-12p40(Oppmann et al., 2000), our data suggested that IL-12p40, but not IL-23p19, is the limiting factor for the production of biologically active IL-23 by DCs in psoriatic skin.

We then studied the lineage of CCR7$^+$ DC in psoriatic skin, as these cells were reported to arise from both cDC1 and cDC2, and possibly DC3(Kvedaraite and Ginhoux, 2022). We characterized cDC1, cDC2, DC3 and CCR7$^+$ DC based on cDC1, cDC2 and DC3 scores determined according to the following formula: sum [gene values of (cDC1 markers, cDC2 markers, or DC3 markers) in an individual cell]/sum (22,438 annotated gene values in the same cell). Our data suggested that CCR7$^+$ DC in psoriatic skin were similar to cDC2 at the transcriptional level (**Figure 2F**). Collectively, our results indicated that CCR7$^+$ DC likely arise from cDC2 and provide all the key signals required to activate the T17 cell response in psoriasis.

CCR7$^+$ DC ablation disables IL-23 signaling in psoriasis-like mouse skin

We next used the IL-23-dependent IMQ-induced mouse model of psoriasis to confirm that CCR7$^+$ DC is the primary source of competent IL-23(van der Fits et al., 2009). We collected mouse skin samples treated with IMQ for 2 days or 5 days and untreated skin as a control for scRNA-seq. After extraction of the myeloid cells, the integrated data were sub-clustered in an unbiased manner and we named the cells according to their countermarks (**Figures S7A** and **3A**). In accordance with the findings in human psoriatic skin, CCR7$^+$ DC, but not other types of DCs or monocytes, expressed both the *Il23a* and

Il12b transcripts (**Figure 3B**). Our similarity analysis suggested that CCR7^{+} DC resembled cDC2 in both normal and IMQ-treated mouse skin (**Figure 3C**). Previous studies demonstrated that Mgl2^{+} myeloid cell deletion abrogated IL-23 in psoriasis-like skin inflammation(Kim et al., 2018; Whitley et al., 2022), while our data suggested that skin *Mgl2*$^{+}$ myeloid cells consisted of *Ear2*$^{+}$ DC3 and *Apod*$^{+}$ cDC2, with the latter cells possibly giving rise to *Il4i1*$^{+}$CCR7^{+} DC that produced IL-23 (**Figures S7A**, **3C** and **3D**).

To study IL-23 in a loss-of-CCR7^{+} DC setting, we generated *Il4i1*^{cre} mice and crossed them with ROSA26iDTR mice (**Figure 3E**). Injection of the *Il4i1*^{cre} DTR mice with diphtheria toxin (DT) resulted in the deletion of IL-23-producing CCR7^{+} DC, as confirmed by both scRNA-seq and flow cytometric analysis (CD45^{+}Ly6G^{-}CD11c^{+}MHCII^{+}CD64^{-}CD326^{-}XCR1^{-}CD200^{+}) of mouse skin treated with IMQ for 3 days (**Figures 3F-3I** and **S7B**). Enzyme-linked immunosorbent assay (ELISA) of the IL-23 heterodimer further confirmed that CCR7^{+} DC deletion abrogated IL-23 expression in IMQ-treated murine skin (**Figure 3J**). Thus, we demonstrated that CCR7^{+} DC are the source of IL-23 in the IMQ-induced mouse model of psoriasis, which is consistent with the scenario in human psoriasis.

IL23a overexpression in Il4i1^{+} cells elicits psoriasis-like skin inflammation

To study CCR7^{+} DC in a gain-of-function setting, we crossed *Il4i1*^{cre} mice with *CAG-LSL-IL23a* mice and overexpressed IL-23a in CCR7^{+} DC (**Figure 4A**). Importantly, *Il4i1-Il23a*^{OE} mice developed scaly plaques on the hairless skin regions, including ears and tails, at 12 weeks of age (**Figure 4B**). Histological examination of the skin lesions showed epidermal hyperplasia (acanthosis) with loss of the granular layer in the epidermis together with accumulation of microabscesses on the surface of the thickened epidermis and massive cellular infiltrates in the dermis (**Figure 4C**). Immunohistochemical analysis of Krt6, Krt5, Krt1/10, Ki67 and filaggrin further

confirmed the hyperproliferation and abnormal differentiation of keratinocytes in *Il4i1-Il23a*^{OE} mice (**Figure 4D**). We also crossed *Itgax*^{cre} mice with *CAG-LSL-IL23a* mice to achieve IL-23a overexpression in CD11c^{+} pan DC. The resulting *Itgax-Il23a*^{OE} mice developed systemic inflammatory phenotypes, although their psoriasis-like skin inflammatory features, especially acanthosis, were not as prominent as those of the *Il4i1-Il23a*^{OE} mice (**Figure S8A**). Thus, we showed that *Il4i1-Il23a*^{OE} mice recapitulate key pathological characteristics of human psoriasis in a cell-type-restricted fashion.

Psoriasis mouse models, including IMQ-induced and recombinant IL-23-mediated skin inflammation, differ from human psoriasis in that IL-17 is produced mainly by γδT cells rather than αβT cells in these models(Cai et al., 2011; Mabuchi et al., 2011). Notably, *Il4i1-Il23a*^{OE} mouse skin contained significantly more αβT cells than *Itgax-Il23a*^{OE} mouse skin (**Figure 4E**), and IL-17a^{+} T cells (T17) were mostly αβT cells in the skin lesions of *Il4i1-Il23a*^{OE} mice (**Figure S8B**). Moreover, transcriptomic profiling of *LSL-Il23a*, *Itgax-Il23a*^{OE} and *Il4i1-Il23a*^{OE} mouse skin revealed human psoriasis-like gene alterations in *Il4i1-Il23a*^{OE} mice, with the differentially expressed genes (DEGs) enriched in epidermis development (*Krt6a*, *Krt6b*, *Krt16* and *Krt17*), αβT cell activation (*Trac*, *Trbc1*, *Trbc2*, *Cd28* and *Gpr18*), and immune response (*Il12b*, *Il17a*, *Il17f* and *Il22*, **Figure 4F**). The DEGs in *Il4i1-Il23a*^{OE} mouse skin resembled those in human psoriatic skin when analyzed using a linear regression model, which showed a stronger coefficient of determination (R) compared to those in IMQ-treated or *Itgax-Il23a*^{OE} mouse skin (**Figure 4G**). Collectively, our findings demonstrated that IL-23a overexpression in Il4i1^{+} cells leads to a psoriasis-like mouse model characterized by αβT cell activation, thus highlighting the central role of CCR7^{+} DC in the cellular and molecular program that drives psoriasis.

Il4i1-Il23a^{OE} mice develop psoriatic arthritis-like symptoms

Up to 30% of psoriasis patients develop psoriatic arthritis (PsA), which is diagnosed according to inflammatory musculoskeletal features in the joints, entheses or spine in the presence of skin and/or nail psoriasis(FitzGerald et al., 2021). We observed digit swelling (dactylitis) and paw swelling in *Il4i1-Il23a*^{OE} mice after 12 weeks of age, and histological examination of the paws confirmed transformation of the synovial lining into hyperplastic pannus in the joints (**Figures 5A** and **5B**). Bulk RNA-seq of the metacarpal and phalangeal bones of the fore paws confirmed the presence of bone resorption, as revealed by the increased expression of *Oscar, Fcgr4, Dcstamp* and *Adam8*. Furthermore, key drivers of bone resorption including *Tnfsf11* (RANKL), *Ocstamp, Tyobp, Itgb3, Slc9b2* were significantly enriched in the bones and joints of *Il4i1-Il23a*^{OE} mice, indicating that this effect was due to osteoclast activation (**Figure 5C**). The data further revealed neutrophil infiltration and IFN-γ-induced signaling in the bones and joints of *Il4i1-Il23a*^{OE} mice, suggesting a resemblance to the immunophenotype involving mixed type 1 and type 17 T cell responses in human PsA (**Figure 5C**)(FitzGerald et al., 2021). We then visualized the structural damages of hind paws from 25~29-week-old *Il4i1-Il23a*^{OE} as compared to *LSL-Il23a* control mice using microCT (**Figure 5D**). Scanning of the intersecting surfaces of the metatarsal bones showed decreased cortical bone thickness (Ct.Th), cortical bone area (Ct.Ar) and bone volume to total volume ratio (BV/TV) in *Il4i1-Il23a*^{OE} mice (**Figures 5E** and **5F**). These data clearly demonstrated bone destruction of the metatarsophalangeal joint, which is the most affected site in PsA patients(Wang et al., 2023). Thus, *Il4i1-Il23a*^{OE} mice were validated as a model of PsA, with pathological features including T cell activation, osteoclast differentiation, and bone resorption in the bones and joints.

Spatial crosstalk between CCR7^{+} DC, CD161^{+} T cells and KRT17^{+} keratinocytes in psoriasis

Having demonstrated that CD161^{+} T cell-derived IL-17 regulated KRT17^{+} keratinocytes,

and CCR7$^+$ DC-derived IL-23 is a prerequisite of IL-17 production, we next explored the relationships between these three cell types and visualized CD161$^+$ T cells (*KLRB1*$^+$) and CCR7$^+$ DC (*LAMP3*$^+$) in psoriatic skin sections. Importantly, in psoriatic epidermis, CCR7$^+$ DC were co-localized with CD161$^+$ T cells (**Figures 6A** and **S9**). Immunofluorescence staining of LAMP3, CD161 and KRT17 confirmed the spatial transcriptome data (**Figure 6B**), in that CCR7$^+$ DC, CD161$^+$ T cells, and KRT17$^+$ keratinocytes form a spatial cellular module that sustains the IL-23-T17 inflammatory axis in psoriasis. To further clarify the mechanism underlying the formation of such a module, we studied cell chemotaxis in psoriatic skin by predicting cell-cell ligand-receptor interactions using CellPhoneDB(Efremova et al., 2020). Importantly, epidermal CCR7$^+$ DC expressed *CCL19*, which is required to recruit dermal CCR7$^+$ DC, and *CXCL16*, which attracts dermal and epidermal CD161$^+$ T cells (**Figures 6C** and **6D**). Taken together, our data supported a working model in which CCR7$^+$ DC first reach the epidermis to initiate the IL-23-dominated inflammatory program that involves the subsequent recruitment of CD161$^+$ T cells and the production of IL-17.

DISCUSSION

In this study, we reveal the immune landscapes of the epidermis and dermis in psoriasis compared with homeostasis. We show that the hyperproliferative keratinocytes in psoriasis, which undergo a disordered differentiation program, are characterized by ectopic overexpression of KRT17 in their most differentiated state. Localized in the outermost layers of psoriatic epidermis, $KRT17^+$ keratinocytes express high levels of IL-17-downstream gene signatures, which is attributed to their spatial proximity to IL-17-producing $CD161^+$ T cells. In psoriatic skin, $CCR7^+$ DC, which are likely differentiated from cDC2, enter the epidermis and recruit $CD161^+$ T cells. Importantly, $CCR7^+$ DC readily provide first, second and third signals (IL-23) that activate $CD161^+$ T cells and induce the production of IL-17. The intimate co-localization of $CCR7^+$ DC, IL-17-producing $CD161^+$ T cells, and $KRT17^+$ keratinocytes therefore indicates a type 17 spatial module in psoriatic epidermis, suggesting pathogenic roles of cells within the module, as well as the therapeutic potential of harnessing this module in psoriasis.

The cellular source of IL-23 in psoriatic skin is controversial. Several studies showed that monocytes/macrophages or monocyte-derived DCs express IL-23A(Cai et al., 2011; Fuentes-Duculan et al., 2010; Hansel et al., 2011), while more recently, Nakamizo et al. reported that $CD14^+$ DC3 express a high level of IL-23A in human psoriatic skin(Nakamizo et al., 2021). Studies on mouse models of psoriasis suggested that Mgl2 $(CD301b)^+$ cDC2 were the major source of IL-23(Kim et al., 2018; Whitley et al., 2022); however, there is no human homolog of the *Mgl2* gene. Due to the enigma related to the source of IL-23, the upstream regulatory mechanisms of IL-23 production are ill-defined, thus hindering the development of targeted therapies focusing on modulating IL-23 expression. In this study, we showed that IL-23A is indeed expressed by many monocyte and DC populations with $CD14^+$ DC3 harboring the maximum transcripts, while IL-12B

is dominantly expressed by CCR7^{+} DC in human psoriatic skin. Given that IL-23A cannot be secreted and thus, is not biologically active without binding to IL-12B(Oppmann et al., 2000), our findings demonstrate that the cellular specificity of IL-23 production is determined by IL-12B rather than IL-23A, and that CCR7^{+} DC are the main producer of IL-23 in psoriasis.

Here, we employed scRNA-seq to confirm that CCR7^{+} DC predominantly produce IL-23 in the IMQ-induced mouse model of psoriasis. Notably, *Mgl2*$^{+}$ DC consist of *Ear2*$^{+}$ DC3 and *Apod*$^{+}$ cDC2, and the latter possibly differentiate into CCR7^{+} DC in psoriasis-like skin lesions. Because CCR7^{+} DC specifically express high levels of *Il4i1*, we generated *Il4i1*^{cre} mice and crossed them with both ROSA26iDTR and *LSL-IL23a* mouse strains to study IL-23 production in both loss and gain-of-function settings. DT-induced deletion of CCR7^{+} DC in *Il4i1*^{cre} DTR mice abrogated IMQ-induced IL-23 expression, implicating CCR7^{+} DC as the main source of IL-23 in psoriasis-like mouse skin. On the other hand, IL-23a overexpression in Il4i1^{+} cells recapitulates key features of human psoriasis including αβT cell-dominated IL-17 production and the propensity to develop PsA. The observation that IL-23a overexpression in CD11c^{+} pan DC does not drive psoriasis-like skin inflammation reveals not only a unique pathogenic role of CCR7^{+} DC, but also offers a valuable mouse model suitable for the investigation of IL-23 generation mechanisms. In addition, this model provides opportunities for the design of new therapies targeting IL-23-producing cells to treat a broad spectrum of auto-inflammatory diseases. Thus, our model represents the first step in developing the next generation of targeted drugs for the purpose of achieving longer term disease remission.

Other than producing IL-23, psoriatic CCR7^{+} DC express high levels of antigen presentation molecules, including *HLA-A*, *HLA-B*, *HLA-C*, *CD1B*, and *CD1E*, and co-stimulatory signals, including *CD80*, *CD86*, and *CD40*. These data suggest the strong

antigen-presenting capacity of $CCR7^+$ DC and their central role in maintaining the T17 cell response, which is further evidenced by the co-localization of $CCR7^+$ DC, $CD161^+$ T cells and $KRT17^+$ keratinocytes. This "type 17 module" concept and the fact that psoriasis is strongly associated with HLA polymorphisms highlight the importance of further investigation of antigens presented by $CCR7^+$ DC and then recognized by $CD161^+$ T cells, which may elucidate the exact cause of auto-inflammation in psoriasis and the mechanisms of relapse.

ACKNOWLEDGMENTS

This work was supported by the National Natural Science Foundation of China Original Exploration Program (82050009), the National Key Research and Development Program of the Ministry of Science and Technology (2020YFA0112900), the National Science Foundation of China (81930088, 82173417 [Y.S.], 82203914 [F.L.] and 82373470 [F.L.]), Shanghai Scientific and Technological Innovation Action Plan (22140903100, 22QA1407600 [F.L.] and 23ZR1480700 [F.L.]), SJTU Trans-med Awards Research (20210102), and Innovative Research Team of High-Level Local Universities in Shanghai [by H.W. if not otherwise noted].

AUTHOR CONTRIBUTIONS

Conceptualization, H.W., Y.S. and F.L.; Investigation, Y.S., F.L., X.C., Z.W., X.Y., L.S. and Z.L.; Data curation, Y.S.; Writing – original draft, F.L.; Writing – review & editing, H.W., F.G., F.L. and Y.S.; Funding acquisition, H.W., Y.S. and F.L.; Resources, Z.W. and Y-L.S.; Supervision, H.W.; Project administration, H.W.

DECLARATION OF INTERESTS

The authors declare no competing interests.

FIGURE LEGENDS

Figure 1. Altered T cell sub-clusters and type 17 biased response in psoriatic skin.

(**A**) UMAP dimensional reduction and sub-clustering of T cells from psoriatic epidermis samples (n = 6), psoriatic dermis samples (n = 6), healthy epidermis samples (n = 4) and healthy dermis samples (n = 4) and split by sample types.

(B) Heatmap of signature genes in T cell sub-clusters in (A).

(**C**) Percentages of *IL17A*$^+$, *IL17F*$^+$ and *IL26*$^+$ T cells in *KLRB1*$^+$ T cells in psoriatic

samples and healthy controls. Data represent the 25th to 75th percentiles (whiskers showing min to max). *P*-values were determined by two-tailed unpaired *t*-test. ns, not significant.

(**D**) Percentages of *CD4*$^{+}$*IL17A*$^{+}$, *CD8*$^{+}$*IL17A*$^{+}$, *CD4*$^{+}$*CD8*$^{+}$*IL17A*$^{+}$ and *CD4*$^{-}$*CD8*$^{-}$*IL17A*$^{+}$ T cells in *KLRB1*$^{+}$ T cells in psoriatic samples and healthy controls. Data represent the 25th to 75th percentiles (whiskers showing min to max). *P*-values were determined by two-tailed unpaired *t*-test. ns, not significant.

(**E**) GSEA of IL-17A-downstream gene signatures in keratinocyte sub-clusters of psoriatic epidermis. Normalized enrichment score (NES) values were calculated from sub-clusters on the vertical axis versus sub-clusters on the horizontal axis. The numbers represent the nominal (NOM) *P*-values.

(F) Spatial feature-plots of indicated genes in psoriatic skin section from a patient.

(**G**) Spatial feature-plots of *IL17A* and *IL17F* in psoriatic skin section from a patient and merged with *KRT17*$^{+}$ (*KRT17* expression > 30) spots.

(**H**) Representative image of RNAscope detection of *IL17A* combined with immunofluorescence of KRT17 in psoriatic skin (n = 3). Scale bar, 25 μm. Data are representative of two independent experiments.

Figure 2. CCR7^{+} DC dominantly produce IL-23 in psoriatic skin.

(**A**) UMAP dimensional reduction and sub-clustering of DCs and monocytes from psoriatic epidermis samples (n = 6), psoriatic dermis samples (n = 6), healthy epidermis samples (n = 4) and healthy dermis samples (n = 4) and split by sample types.

(**B**) Heatmaps of genes associated with the indicated functions in different DC and monocyte subtypes of psoriatic skin.

(**C**) Cell percentages expressing *IL12A*, *IL12B* and *IL23A* and average expression of these genes in different DC and monocyte subtypes of psoriatic skin.

(**D**) Representative image of RNAscope detection of *CD200*, *IL12B* and *Il23A* mRNAs in

psoriatic skin (n = 3). Scale bar, 25 μm. Data are representative of three independent experiments.

(**E**) Flow cytometry showing the percentages of $CD1B^{+}CD200^{+}$ cells in $IL\text{-}12p40^{+}IL\text{-}23p19^{+}$, $IL\text{-}12p40^{-}IL\text{-}23p19^{+}$ and $IL\text{-}12p40^{-}IL\text{-}23p19^{-}$ cells among $CD45^{+}CD11C^{+}$ cells in psoriatic skin samples (n = 3). Data represent the mean ± SEM. Data are representative of three independent experiments.

(**F**) Three-dimensional scatter plots showing cDC1 scores, cDC2 scores and DC3 scores of cDC1, cDC2, DC3 and $CCR7^{+}$ DC in psoriatic skin. The scores were calculated as the fraction of RNA in a cell belonging to genes in the list shown in Supplementary Table 1.

Figure 3. $CCR7^{+}$ DC ablation disables IL-23 signaling in psoriasis-like mouse skin.

(**A**) UMAP dimensional reduction and sub-clustering of scRNA-seq data for sorted $CD45^{+}Ly6G^{-}CD3^{-}CD19^{-}$ cells from mouse ears treated or not with IMQ for 2 days or 5 days.

(**B**) Feature-plots of *Il23a* and *Il12b* expression in (A).

(**C**) Three-dimensional scatter plots showing cDC1 scores, cDC2 scores and DC3 scores of cDC1, cDC2, DC3 and $CCR7^{+}$ DC from mouse ears treated or not with IMQ for 2 days. The scores are calculated as the fraction of RNA in a cell belonging to genes in the list shown in Supplementary Table 1.

(**D**) Violin-plots of indicated genes in different myeloid cells from mouse ears treated with IMQ for 2 days.

(**E**) The strategy to delete $CCR7^{+}$ DC and schematic diagram of DT and IMQ treatment.

(**F**) UMAP dimensional reduction and sub-clustering of scRNA-seq data for ears from IMQ-treated *Il4i1*^{cre}DTR mice pre-injected with DT or not.

(**G**) Proportions of different cell types in $CD45^{+}$ cells of ears from IMQ-treated *Il4i1*^{cre}DTR mice pre-injected with DT or not.

(**H**) Feature-plots of *Il23a* and *Il12b* expression in (F).

(**I**) Flow cytometry showing the percentages of $CCR7^+$ DC in cDC2 ($CD45^+Ly6G^-CD11c^+MHCII^+CD64^-CD326^-XCR1^-$) of ears from *Il4i1*^{cre}DTR mice treated under the indicated conditions (n = 3~5). Data represent the 25th to 75th percentiles (whiskers showing min to max). *P*-values were determined by one-way ANOVA. Data are representative of two independent experiments.

(**J**) ELISA quantification of IL-23 in ears from *Il4i1*^{cre}DTR mice treated under the indicated conditions (n = 3~5). Data represent the 25th to 75th percentiles (whiskers showing min to max). *P*-values were determined by one-way ANOVA. Data are representative of two independent experiments.

Figure 4. *Il23a* overexpression in $CCR7^+$ DC elicits psoriasis-like skin disease.

(**A**) Strategy for developing *Il4i1-Il23a*^{OE} mice.

(**B**) Representative macroscopic views of skin lesions of 12-week-old *Il4i1-Il23a*^{OE} mice (n = 5).

(**C**) Representative H&E images and quantification of acanthosis in 12-week-old *Il4i1-Il23a*^{OE} mice (n = 6) and *LSL-Il23a* mice (n = 5). Scale bar, 50 μm. Data represent the 25th to 75th percentiles (whiskers showing min to max). *P*-values were determined by two-tailed unpaired *t*-test.

(**D**) Representative immunofluorescence images of Krt6, Krt5, Krt1/10, Ki67 and Filaggrin of ears from 12-week-old *LSL-Il23a* mice and *Il4i1-Il23a*^{OE} mice (n =3). Scale bar, 25 μm.

(**E**) Flow cytometry showing the percentages of $CD45^+TCR\beta^+$ cells in live cells of ears from 12-week-old *LSL-Il23a* mice (n = 8), *Itgax-Il23a*^{OE} mice (n = 6) and *Il4i1-Il23a*^{OE} mice (n = 6). Data represent the 25th to 75th percentiles (whiskers showing min to max). *P*-values were determined by one-way ANOVA.

(**F**) Heatmap of selected genes from bulk RNA-seq data from the ears of 12-week-old *LSL-Il23a* mice (n = 3), *Itgax-Il23a*^{OE} mice (n = 3) and *Il4i1-Il23a*^{OE} mice (n = 3). The GO categories are indicated.

(**G**) Linear correlations between mouse transcriptional profiles (model versus control) and human transcriptional profile (psoriasis versus healthy control). Genes identified as DEGs ($|\log2FC| \geq 1$ and $p < 1\times10^{-6}$) in the human dataset (GSE54456) were used (Li et al., 2014), and mouse genes were joined by case-insensitive gene symbol matching. The gene expression levels of *Il4i1-Il23a*^{OE} mice or *Itgax-Il23a*^{OE} mice versus *LSL-Il23a* mice were from our data, and the gene expression levels of IMQ-treated C57BL/6J mice versus control mice were from GSE86315 (Swindell et al., 2017).

Data (**B**-**E**) are representative of three independent experiments.

Figure 5. *Il4i1-Il23a*^{OE} mice develop psoriatic arthritis-like symptoms.

(**A**) Representative macroscopic views of the paws of 16-week-old *LSL-Il23a* mice (n = 5) and *Il4i1-Il23a*^{OE} mice (n = 5).

(**B**) Representative H&E images of the hind paws from 16-week-old *LSL-Il23a* mice (n = 3) and *Il4i1-Il23a*^{OE} mice (n = 6). Scale bar, 100 μm.

(**C**) Heatmap of selected genes from bulk RNA-seq data of the metacarpal and phalangeal bones from 16-week-old *LSL-Il23a* mice (n = 3) and *Il4i1-Il23a*^{OE} mice (n = 4). The GO categories are indicated.

(**D**) Representative microCT images of the hind paws from 25~29-week-old *LSL-Il23a* mice (n = 8) and *Il4i1-Il23a*^{OE} mice (n = 11). Scale bar, 1 mm.

(**E**) Representative microCT images of the metatarsal bones proximal to the metatarsophalangeal joints from 25~29-week-old *LSL-Il23a* mice (n = 8) and *Il4i1-Il23a*^{OE} mice (n = 11). II, III and IV represent three different toes of the mice. Scale bar, 1 mm.

(**F**) Quantification of bone structural parameters of 25~29-week-old *LSL-Il23a* mice (n =

8) and *Il4i1-Il23a*^{OE} mice (n = 11) shown in (E). Data represent the 25th to 75th percentiles (whiskers showing min to max). Ct.Th, cortical bone thickness; Ct.Ar, cortical bone area; Tt.Ar, total area of the cross section; BV/TV, bone volume to total volume ratio; ns, not significant.

Data (**A**, **B** and **D-F**) are representative of three independent experiments.

Figure 6. CCR7^{+} DC define a type 17 spatial module in psoriatic epidermis.

(**A**) Spatial feature-plots of *KLRB1* and *LAMP3* in psoriatic skin section from a patient.

(**B**) Representative immunofluorescent labeling of CD161, LAMP3 and KRT17 in psoriatic skin (n = 3). Data are representative of two independent experiments.

(**C**) Chemokine receptor-ligand pairs across cell subpopulations within psoriatic skin. All interactions shown are statistically significant ($p < 0.05$), and arrows denote directionality from ligand to receptor.

(**D**) A working model of chemotaxis of CCR7^{+} DC and CD161^{+} T cells in psoriatic skin.

Figure S1. A single-cell transcriptomic landscape in the skin of patients with psoriasis and healthy donors.

(**A**) Schematic overview of skin samples processed for 3'-barcoded scRNA-seq and spatial transcriptome.

(**B**) General information of patients with psoriasis and healthy donors.

(**C**) Representative flow cytometry plots showing the gating strategy of all live cells in the epidermis and CD45^{+} live leukocytes in the dermis.

(**D**) UMAP dimensional reduction and cell type clustering of 3'-barcoded scRNA-seq data containing epidermal cells and dermal CD45^{+} leukocytes from patients with psoriasis and healthy donors.

(**E**) Feature-plots of marker genes for cell clustering in (D).

Figure S2. Sub-clustering of keratinocytes in psoriatic and normal skin.

(A) UMAP dimensional reduction and sub-clustering of keratinocytes from psoriatic epidermis samples (n = 6) and healthy controls (n = 4).

(**B**) Heatmap of signature genes in keratinocyte sub-clusters shown in (A).

(**C**) KRT genes in keratinocyte sub-clusters of psoriatic epidermis samples and healthy controls.

(**D**) Pseudo-time trajectories of keratinocytes in psoriatic epidermis samples and healthy controls.

Figure S3. Characterization of *KLRB1*$^+$ T cells.

(**A**) Feature-plots of indicated genes in T cells.

(**B**) Percentages of *CD4*$^+$, *CD8*$^+$, *CD4*$^+$*CD8*$^+$ and *CD4*$^-$*CD8*$^-$ T cells in *KLRB1*$^+$ T cells from psoriatic samples and healthy controls. Data represent the 25th to 75th percentiles (whiskers showing min to max). ns, not significant.

Figure S4. Spatial distribution of IL-17A-downstream signatures.

(**A**, **B**) Spatial feature-plots of indicated genes in psoriatic skin sections.

(**C**) Representative immunofluorescence images of KRT17 and IL17RA expression in normal (n = 3) and psoriatic skin sections (n = 5). Data are representative of two independent experiments.

Figure S5. Co-localization of IL-17 and KRT17$^+$ keratinocytes in psoriatic epidermis.

Spatial feature-plots of *IL17A* and *IL17F* in skin sections from psoriatic patients and healthy donors and merged with KRT17$^+$ (*KRT17* expression > 30) spots.

Figure S6. DC and monocyte subtypes in psoriatic and normal skin.

(**A**) Heatmap of signature genes in DC and monocyte subtypes in Figure 3A.

(**B**) Representative flow cytometry plots of IL-12p40^{+}IL-23p19^{+}, IL-12p40^{-}IL-23p19^{+} and IL-12p40^{-}IL-23p19^{-} cells in CD45^{+}CD11C^{+} cells from psoriatic skin samples (n = 3).

(**C**) Percentages of IL-12p40^{+}IL-23p19^{+}, IL-12p40^{-}IL-23p19^{+} and IL-12p40^{-}IL-23p19^{-} cells in CD45^{+}CD11C^{+} cells from psoriatic skin samples (n = 3). Data represent the mean ± SEM. Data are representative of three independent experiments.

Figure S7. Characterization of myeloid cells in IMQ-induced murine skin.

(**A**) Feature-plots of indicated genes in CD45^{+}Ly6G^{-}CD3^{-}CD19^{-} myeloid cells from mouse ears treated or not with IMQ for 2 days or 5 days.

(**B**) Representative flow cytometry plots of CCR7^{+} DC subsets in cDC2 (CD45^{+}Ly6G^{-}CD11c^{+}MHCII^{+}CD64^{-}CD326^{-}XCR1^{-}) of ears from *Il4i1*^{cre}DTR mice treated under the indicated conditions (n = 3~5). Data are representative of two independent experiments.

Figure S8. Pathological features of ear skin in *Itgax-Il23a*^{OE} mice.

(**A**) Representative H&E images and quantification of acanthosis of 12-week-old *Itgax-Il23a*^{OE} mice (n = 5) and *LSL-Il23a* mice (n = 5). Scale bar, 50 μm. Data represent the 25th to 75th percentiles (whiskers showing min to max). *P*-value was determined by two-tailed unpaired *t*-test.

(**B**) Flow cytometry showing the percentages of TCRβ^{+} cells in CD3^{+}IL-17a^{+} T cells (T17) of ears from 12-week-old *LSL-Il23a* mice (n = 8), *Itgax-Il23a*^{OE} mice (n = 6) and *Il4i1-Il23a*^{OE} mice (n = 6). Data represent the 25th to 75th percentiles (whiskers showing min to max). *P*-values were determined by one-way ANOVA.

Data are representative of three independent experiments.

Figure S9. Co-localization of KLRB1 and LAMP3 in psoriatic epidermis.

Spatial feature-plots of *KLRB1*and *LAMP3* in skin sections from psoriatic patients and the merged plots.

EXPERIMENTAL MODEL AND SUBJECT DETAILS

Human subjects

Psoriatic skin samples were obtained by punch biopsy from patients under local lidocaine anesthesia. Normal adult human skin specimens were obtained from healthy donors undergoing plastic surgery. All participants provided written informed consent. This study was performed in accordance with the principles of the Declaration of Helsinki and approved by the Research Ethics Boards of Shanghai General Hospital, China (No. 2018KY239).

Animals

C57BL/6 mice were purchased from Shanghai SLAC Laboratory Animal Co., Ltd. *Il4i1-2A-Cre* (*Il4i1*^{cre}) mice and *R26-CAG-LSL-Il23a-IRES-EGFP* (*LSL-Il23a*) mice were produced by Shanghai Model Organisms Co., Ltd. *ROSA26-LSL-DTR* (ROSA26iDTR) mice and *Itgax*^{cre} mice were obtained from Cyagen Co., Ltd. The mice were bred and maintained under specific pathogen-free (SPF) conditions. Age-matched and sex-matched mice were used for all the experiments in accordance with the National Institutes of Health Guide for the Care and Use of Laboratory Animals with the approval (SYXK-2019-0028) of the Scientific Investigation Board of Shanghai General Hospital. Throughout these experimental studies, all efforts were made to alleviate any suffering and the mice were euthanized by CO_2 inhalation.

METHOD DETAILS

Single-cell transcriptomics

Sample preparation, library production and RNA sequencing

Fresh skin biopsies were placed in saline at 4□ prior to processing. The epidermis was

separated from the dermis by dispase II digestion overnight at 4□. Single-cell suspensions were generated by enzyme digestion as previously reported(Lou et al., 2020) and analyzed by flow cytometry to exclude doublets, debris, and DAPI-positive dead cells. For dermis samples, $CD45^+$ cells were sorted for subsequent processing. Sorted cells were centrifuged and resuspended in 0.04% BSA in phosphate-buffered saline (PBS). Chromium Single Cell 3' v3 (10× Genomics) libraries were prepared using the Chromium Controller according to the manufacturer's instructions. The resulting libraries were sequenced with the Illumina NovaSeq 6000 platform. Trimmed data were processed using the CellRanger (version 3.0, 10× Genomics) and further filtered, processed, and analyzed using the Seurat package (version 4.3.0)(Butler et al., 2018).

Data processing and clustering with Seurat

Cells with fewer than 200 genes, more than 5,000 genes, or more than 5% mitochondria content were removed. Doublets were predicted using DoubletFinder and removed(McGinnis et al., 2019). The filtered data were normalized using a scaling factor of 10,000 to generate transcripts per kilobase million (TPM)-like values. We integrated the filtered samples using the FindIntegrationAnchors and IntegrateData functions with default parameters (dimensionality = 30). The top 2,000 most variable genes were selected using the FindVariableFeatures function and the genes were then used for principal component analysis (PCA). The number of PCs for clustering was selected based on the 'Elbow plot' of different datasets. Clustering was performed using the FindClusters function with a resolution selected for different datasets. Results were visualized using the Seurat package.

Pseudo-time trajectory analysis using Monocle

Keratinocytes pre-clustered and labeled according to the countermark genes were used as an input for Monocle 2 in the pseudo-time trajectory analysis(Trapnell et al., 2014). Genes with expression levels lower than 0.1 and genes expressed by fewer than 10 cells were removed. The remaining cells were clustered in an unsupervised manner and DEGs

were identified using the differentialGeneTest function. The top 1,000 significant DEGs were selected as the ordering genes. The DDRTree algorithm was used for dimension reduction and BEAM was used to identify the genes driving the transition in pseudo-time.

Spatial transcriptomics

Fresh skin biopsies from healthy donors and patients with psoriasis were embedded in optical cutting tissue (OCT) compound and snap-frozen on dry ice. Skin sections (10 μm thick) were prepared using a cryostat microtome and mounted onto Visium slides (Visium Spatial Tissue Optimization Slide & Reagent kit, 10× Genomics). After hematoxylin and eosin (H&E) staining, bright-field images were obtained. Optimized permeabilization (for 24 min) and tissue removal were conducted on the Visium slides. After reverse transcription, the barcoded cDNA was enzymatically released and collected. The cDNA libraries were then sequenced on the Illumina NovaSeq 6000 platform. The data were processed with the SpaceRanger (version 1.1.0, 10× Genomics) and mapped to the GRCh38-2020-A genome. Results were visualized using the Seurat package (version 4.3.0).

Flow cytometry

Single cell suspensions were generated from the skin of patients with psoriasis, *Il4i1*^{cre} DTR mice, *LSL-Il23a* mice, *Itgax-Il23a*^{OE} mice and *Il4i1-Il23a*^{OE} mice as previously reported(Lou et al., 2020). Cells were stained with fluorophore-conjugated antibodies and assayed with a BD LSRFortessa™ or a BD FACSymphony™ A3 cytometer, and the data were analyzed using FlowJo software. For human sample analyses, antibodies against CD45 (clone 2D1) and CD1b (clone SN13) were obtained from BioLegend; CD45 (clone HI30), CD200 (clone MRC OX-104) and CD11C (clone B-ly6) were obtained from BD Biosciences; IL-23p19 (clone 23dcdp), IL-12/IL-23p40 (clone eBioHP40) were obtained from eBioscience. For mouse sample analyses, antibodies against CD45 (clone 30-F11)

were obtained from BioLegend or BD Biosciences; Ly-6G (clone 1A8) and CD200 (clone OX-90) were obtained from BD Biosciences; CD11c (clone N418), TCRbeta (clone H57-597) and MHC Class II (I-A/I-E) (clone M5/114.15.2) were obtained from eBioscience; CD326 (Ep-CAM) (clone G8.8), XCR1 (clone ZET) and CD64 (FcγRI) (clone X54-5/7.1) were obtained from BioLegend.

RNAscope™ Multiplex Fluorescent Assay

Human paraffin sections were dewaxed, and single-molecule fluorescence *in situ* hybridization (FISH) experiments were carried out using an RNAscope™ Multiplex Fluorescent Assay v2 with an RNAscope™ Probe-Hs-IL23A-C3 (ACD cat. 562851-C3), an RNAscope™ Probe-Hs-IL12B-C2 (ACD cat. 402071-C2), an RNAscope™ Probe-Hs-CD200 (ACD cat. 410471), and an RNAscope™ Probe-Hs-IL17A (ACD cat. 310931). The sections were mounted with a fluorescent mounting medium (Sigma-Aldrich cat. DUO82040) and visualized under a confocal microscope (Leica, STELLARIS 8 DIVE).

Mouse models of psoriasis

For the IMQ-induced mouse model of psoriasis, male C57BL/6 mice (aged 7 weeks) were maintained under SPF conditions. The mice received a daily topical dose of 25 mg IMQ cream (5%) (MedShine cat. 120503) per ear for two or five consecutive days before the mice were euthanized and the ears were collected for scRNA-seq. For the *Il4i1*^{cre} DTR mice, 100 μg DT (Sigma-Aldrich cat. D0564) was injected intraperitoneally (i.p.) one day before 25 mg IMQ cream was applied per ear for two days. The mice were then euthanized and the ears were collected for scRNA-seq, flow cytometry and ELISA. After euthanization, ears were collected from *LSL-Il23a*, *Itgax-Il23a*^{OE}, and *Il4i1-Il23a*^{OE} mice (aged 12 weeks) for histological analysis, flow cytometry and bulk RNA-seq, while paws were collected from mice (aged 16 weeks) for histological analysis, microCT and bulk

RNA-seq.

ELISA

Ears from *Il4i1*^{cre} DTR mice were snap-frozen, pulverized, and homogenized for protein extraction using a ProteinExt® Mammalian Total Protein Extraction Kit (Transgen cat. DE101-01). IL-23 heterodimer levels were measured using a Mouse IL-23 Quantikine ELISA Kit (R&D Systems cat. M2300) according to the manufacturer's instructions.

Histological analysis and immunofluorescence

Ears from *LSL-Il23a*, *Itagx-Il23a*^{OE} and *Il4i1-Il23a*^{OE} mice were embedded in paraffin and sectioned (5 μm thick). The sections were stained with H&E, and the pixel size of the epidermal area was measured using the lasso tool in Adobe Photoshop CS4. For immunofluorescence staining, the sections were deparaffinized and retrieval was performed by heating the sections in sodium citrate buffer (pH = 6.0) or Tris-EDTA buffer (pH = 8.0). The sections were blocked for 1 h at room temperature (RT) in PBS containing 1% bovine serum albumin (BSA), 5% goat serum, 0.3% Triton X-100 and stained overnight at 37□ in blocking buffer containing primary antibody (anti-Krt6, Polyclonal, Proteintech cat. 10590-1-AP, 1:200 dilution; anti-Krt5, Clone 2C2, Invitrogen cat. MA5-17057, 1:200 dilution; anti-Krt1/10, Clone LH1, Santa Cruz cat. sc-53251, 1:200 dilution; anti-Ki67, Polyclonal, Servicebio cat. GB111499, 1:500 dilution; anti-Filaggrin, Clone FLG01, GeneTex cat. GTX23137, 1:100 dilution; anti-CD161, Clone 14F1F11, NOVUS Cat. NBP2-14845; anti-DC-LAMP, Colne 1010E1.01, NOVUS Cat, DDX0191P-100, anti-KRT17/CK17/Cytoketatin 17, Clone E3, LS Bio Cat. LS-B7169; anti-KRT17/CK17/ Cytoketatin 17, Polyclonal, LS Bio Cat#LS-B7610). Thereafter, the sections were rinsed three times in PBS and stained with fluorochrome-conjugated secondary antibodies (all from Life Technologies, 1:1,000 dilution) for 1 h at RT in the dark. Sections were also stained with DAPI (BD Biosciences

cat. 564907, 1:2,000 dilution) at RT for 5 min to visualize nuclei. The sections were mounted with a fluorescent mounting medium (Sigma-Aldrich cat. DUO82040) and visualized under a confocal microscope (Leica, STELLARIS 8 DIVE).

Bulk RNA-seq

Ears or peeled metacarpal and phalangeal bones were snap-frozen in liquid nitrogen and pulverized. Total RNA was isolated using RNAiso Reagent (TaKaRa cat. 9108). cDNA libraries were prepared using a VAHTS Universal V8 RNA-seq Library Prep Kit for Illumina (Vazyme cat. NR605-01) according to the manufacturer's instructions and sequenced on a NovaSeq 6000 (Illumina). The adaptor sequences were trimmed from the raw paired-end reads using Skewer(Jiang et al., 2014). The sequences were then aligned to GRCm38 using STAR(Dobin et al., 2013) and assembled using StringTie(Pertea et al., 2015). Gene enrichment analysis (GSEA) was performed to identify enriched pathways(Mootha et al., 2003; Subramanian et al., 2005).

MicroCT

Mouse hind paws were collected and fixed in 4% paraformaldehyde and analyzed by microCT (Venus001, Pingseng Scientific). Bone structural parameters including total area (Tt.Ar), cortical bone thickness (Ct.Th), cortical bone area (Ct.ar) and cortical bone area to total cross-sectional area ratio (Ct.ar/Tt.ar) were calculated using DataViewer software (Bruker). The samples were then decalcified using 10% EDTA and embedded for H&E staining.

QUANTIFICATION AND STATISTICAL ANALYSIS

Data were presented as the 25^{th} to 75^{th} percentiles (whiskers showing min to max) or as the mean ± SEM and analyzed using GraphPad Prism 9. Differences between two groups

were evaluated using Student's *t*-test, and differences between multiple groups were evaluated by analysis of variance (ANOVA) with Geisser-Greenhouse correction. A simple linear regression model was used to analyze the transcriptome correlation between mouse models and human psoriasis.

DATA AVAILABILITY

The sequencing data in this paper are deposited in Genome Sequence Archive (GSA). The bulk RNA sequencing data are deposited under the accession: CRA013603; the human single-cell transcriptomics data are deposited under the accessions: HRA003418 and HRA006130; the human spatial transcriptomics data are deposited under the accession: HRA006129.

REFERENCES

Amschler, K., Phillip, S., Mohr, J., Wilsmann-Theis, D., Poortinga, S., Gerdes, S., and Mössner, R. (2020). Long-term follow-up of 22 psoriatic patients treated with ixekizumab after failure of secukinumab. Dermatol Online J *26*.

Anderson, D.A., 3rd, Dutertre, C.A., Ginhoux, F., and Murphy, K.M. (2021). Genetic models of human and mouse dendritic cell development and function. Nat Rev Immunol *21*, 101-115.

Armstrong, A.W., and Read, C. (2020). Pathophysiology, Clinical Presentation, and Treatment of Psoriasis: A Review. JAMA *323*, 1945-1960.

Becht, E., McInnes, L., Healy, J., Dutertre, C.A., Kwok, I.W.H., Ng, L.G., Ginhoux, F., and Newell, E.W. (2018). Dimensionality reduction for visualizing single-cell data using UMAP. Nat Biotechnol.

Bito, T., Nishikawa, R., Hatakeyama, M., Kikusawa, A., Kanki, H., Nagai, H., Sarayama, Y., Ikeda, T., Yoshizaki, H., Seto, H., *et al.* (2014). Influence of neutralizing antibodies to adalimumab and infliximab on the treatment of psoriasis. Br J Dermatol *170*, 922-929.

Butler, A., Hoffman, P., Smibert, P., Papalexi, E., and Satija, R. (2018). Integrating single-cell transcriptomic data across different conditions, technologies, and species. Nat Biotechnol *36*, 411-420.

Cai, Y., Shen, X., Ding, C., Qi, C., Li, K., Li, X., Jala, V.R., Zhang, H.G., Wang, T., Zheng, J., and Yan, J. (2011). Pivotal role of dermal IL-17-producing gammadelta T cells in skin inflammation. Immunity *35*, 596-610.

Cheuk, S., Schlums, H., Gallais Serezal, I., Martini, E., Chiang, S.C., Marquardt, N., Gibbs, A., Detlofsson, E., Introini, A., Forkel, M., *et al.* (2017). CD49a Expression Defines Tissue-Resident CD8(+) T Cells Poised for Cytotoxic Function in Human Skin. Immunity *46*, 287-300.

Cheuk, S., Wiken, M., Blomqvist, L., Nylen, S., Talme, T., Stahle, M., and Eidsmo, L. (2014). Epidermal Th22 and Tc17 cells form a localized disease memory in clinically healed psoriasis. J Immunol *192*, 3111-3120.

Conrad, C., Boyman, O., Tonel, G., Tun-Kyi, A., Laggner, U., de Fougerolles, A., Kotelianski, V., Gardner, H., and Nestle, F.O. (2007). Alpha1beta1 integrin is crucial for accumulation of epidermal T cells and the development of psoriasis. Nat Med *13*, 836-842.

Dobin, A., Davis, C.A., Schlesinger, F., Drenkow, J., Zaleski, C., Jha, S., Batut, P., Chaisson, M., and Gingeras, T.R. (2013). STAR: ultrafast universal RNA-seq aligner. Bioinformatics *29*, 15-21.

Dress, R.J., Liu, Z., and Ginhoux, F. (2020). Towards the better understanding of myelopoiesis using single-cell technologies. Mol Immunol *122*, 186-192.

Efremova, M., Vento-Tormo, M., Teichmann, S.A., and Vento-Tormo, R. (2020). CellPhoneDB: inferring cell-cell communication from combined expression of multi-subunit ligand-receptor complexes. Nat Protoc *15*, 1484-1506.

FitzGerald, O., Ogdie, A., Chandran, V., Coates, L.C., Kavanaugh, A., Tillett, W., Leung, Y.Y., deWit, M., Scher, J.U., and Mease, P.J. (2021). Psoriatic arthritis. Nat Rev Dis Primers *7*, 59.

Fuentes-Duculan, J., Suarez-Farinas, M., Zaba, L.C., Nograles, K.E., Pierson, K.C., Mitsui, H., Pensabene, C.A., Kzhyshkowska, J., Krueger, J.G., and Lowes, M.A. (2010). A subpopulation of CD163-positive macrophages is classically activated in psoriasis. J Invest Dermatol *130*, 2412-2422.

Galluzzo, M., D'Adamio, S., Campione, E., Bianchi, L., and Talamonti, M. (2018). Treating a Multidrug-Resistant Psoriatic HLA-C*18:01 Allele Carrier with Combination Ustekinumab Apremilast Therapy. Mol Diagn Ther *22*, 717-721.

Griffiths, C.E., and Barker, J.N. (2007). Pathogenesis and clinical features of psoriasis. Lancet *370*, 263-271.

Guttman-Yassky, E., Nograles, K.E., and Krueger, J.G. (2011). Contrasting pathogenesis of atopic dermatitis and psoriasis--part II: immune cell subsets and therapeutic concepts. J Allergy Clin Immunol *127*, 1420-1432.

Hansel, A., Gunther, C., Ingwersen, J., Starke, J., Schmitz, M., Bachmann, M., Meurer, M., Rieber, E.P., and Schakel, K. (2011). Human slan (6-sulfo LacNAc) dendritic cells are inflammatory dermal dendritic cells in psoriasis and drive strong TH17/TH1 T-cell responses. J Allergy Clin Immunol *127*, 787-794 e781-789.

Ho, A.W., and Kupper, T.S. (2019). T cells and the skin: from protective immunity to inflammatory skin disorders. Nat Rev Immunol *19*, 490-502.

Jiang, H., Lei, R., Ding, S.W., and Zhu, S. (2014). Skewer: a fast and accurate adapter trimmer for next-generation sequencing paired-end reads. BMC Bioinformatics *15*, 182.

Kim, T.G., Kim, S.H., Park, J., Choi, W., Sohn, M., Na, H.Y., Lee, M., Lee, J.W., Kim, S.M., Kim, D.Y., *et al.* (2018). Skin-Specific CD301b(+) Dermal Dendritic Cells Drive IL-17-Mediated Psoriasis-Like Immune Response in Mice. J Invest Dermatol *138*, 844-853.

Kryczek, I., Bruce, A.T., Gudjonsson, J.E., Johnston, A., Aphale, A., Vatan, L., Szeliga, W., Wang, Y., Liu, Y., Welling, T.H., *et al.* (2008). Induction of IL-17+ T cell trafficking and development by IFN-gamma: mechanism and pathological relevance in psoriasis. J Immunol *181*, 4733-4741.

Kvedaraite, E., and Ginhoux, F. (2022). Human dendritic cells in cancer. Sci Immunol *7*, eabm9409.

Li, B., Tsoi, L.C., Swindell, W.R., Gudjonsson, J.E., Tejasvi, T., Johnston, A., Ding, J., Stuart, P.E., Xing, X., Kochkodan, J.J., *et al.* (2014). Transcriptome analysis of psoriasis in a large case-control sample: RNA-seq provides insights into disease mechanisms. J Invest Dermatol *134*, 1828-1838.

Lou, F., Sun, Y., and Wang, H. (2020). Protocol for Flow Cytometric Detection of Immune Cell Infiltration in the Epidermis and Dermis of a Psoriasis Mouse Model. STAR Protoc *1*, 100115.

Lowes, M.A., Kikuchi, T., Fuentes-Duculan, J., Cardinale, I., Zaba, L.C., Haider, A.S., Bowman, E.P., and Krueger, J.G. (2008). Psoriasis vulgaris lesions contain discrete populations of Th1 and Th17 T cells. J Invest Dermatol *128*, 1207-1211.

Mabuchi, T., Takekoshi, T., and Hwang, S.T. (2011). Epidermal CCR6+ gammadelta T cells are major producers of IL-22 and IL-17 in a murine model of psoriasiform dermatitis. J Immunol *187*, 5026-5031.

Maier, B., Leader, A.M., Chen, S.T., Tung, N., Chang, C., LeBerichel, J., Chudnovskiy, A., Maskey, S., Walker, L., Finnigan, J.P., *et al.* (2020). A conserved dendritic-cell regulatory program limits antitumour immunity. Nature *580*, 257-262.

Masson Regnault, M., Shourick, J., Jendoubi, F., Tauber, M., and Paul, C. (2022). Time to Relapse After Discontinuing Systemic Treatment for Psoriasis: A Systematic Review. Am J Clin Dermatol *23*, 433-447.

McGinnis, C.S., Murrow, L.M., and Gartner, Z.J. (2019). DoubletFinder: Doublet Detection in Single-Cell RNA Sequencing Data Using Artificial Nearest Neighbors. Cell Syst *8*, 329-337.e324.

Mootha, V.K., Lindgren, C.M., Eriksson, K.F., Subramanian, A., Sihag, S., Lehar, J., Puigserver, P.,

Carlsson, E., Ridderstrale, M., Laurila, E., *et al.* (2003). PGC-1alpha-responsive genes involved in oxidative phosphorylation are coordinately downregulated in human diabetes. Nat Genet *34*, 267-273.

Muromoto, R., Hirao, T., Tawa, K., Hirashima, K., Kon, S., Kitai, Y., and Matsuda, T. (2016). IL-17A plays a central role in the expression of psoriasis signature genes through the induction of IκB-ζ in keratinocytes. Int Immunol *28*, 443-452.

Nakamizo, S., Dutertre, C.A., Khalilnezhad, A., Zhang, X.M., Lim, S., Lum, J., Koh, G., Foong, C., Yong, P.J.A., Tan, K.J., *et al.* (2021). Single-cell analysis of human skin identifies CD14+ type 3 dendritic cells co-producing IL1B and IL23A in psoriasis. J Exp Med *218*.

Nestle, F.O., Conrad, C., Tun-Kyi, A., Homey, B., Gombert, M., Boyman, O., Burg, G., Liu, Y.J., and Gilliet, M. (2005). Plasmacytoid predendritic cells initiate psoriasis through interferon-alpha production. J Exp Med *202*, 135-143.

Oppmann, B., Lesley, R., Blom, B., Timans, J.C., Xu, Y., Hunte, B., Vega, F., Yu, N., Wang, J., Singh, K., *et al.* (2000). Novel p19 protein engages IL-12p40 to form a cytokine, IL-23, with biological activities similar as well as distinct from IL-12. Immunity *13*, 715-725.

Ortega, C., Fernandez, A.S., Carrillo, J.M., Romero, P., Molina, I.J., Moreno, J.C., and Santamaria, M. (2009). IL-17-producing CD8+ T lymphocytes from psoriasis skin plaques are cytotoxic effector cells that secrete Th17-related cytokines. J Leukoc Biol *86*, 435-443.

Pertea, M., Pertea, G.M., Antonescu, C.M., Chang, T.C., Mendell, J.T., and Salzberg, S.L. (2015). StringTie enables improved reconstruction of a transcriptome from RNA-seq reads. Nat Biotechnol *33*, 290-295.

Puig, L., Costanzo, A., Munoz-Elias, E.J., Jazra, M., Wegner, S., Paul, C.F., and Conrad, C. (2022). The biological basis of disease recurrence in psoriasis: a historical perspective and current models. Br J Dermatol *186*, 773-781.

See, P., Dutertre, C.A., Chen, J., Günther, P., McGovern, N., Irac, S.E., Gunawan, M., Beyer, M., Händler, K., Duan, K., *et al.* (2017). Mapping the human DC lineage through the integration of high-dimensional techniques. Science *356*.

Subramanian, A., Tamayo, P., Mootha, V.K., Mukherjee, S., Ebert, B.L., Gillette, M.A., Paulovich, A., Pomeroy, S.L., Golub, T.R., Lander, E.S., and Mesirov, J.P. (2005). Gene set enrichment analysis: a knowledge-based approach for interpreting genome-wide expression profiles. Proc Natl Acad Sci U S A *102*, 15545-15550.

Swindell, W.R., Michaels, K.A., Sutter, A.J., Diaconu, D., Fritz, Y., Xing, X., Sarkar, M.K., Liang, Y., Tsoi, A., Gudjonsson, J.E., and Ward, N.L. (2017). Imiquimod has strain-dependent effects in mice and does not uniquely model human psoriasis. Genome Med *9*, 24.

Trapnell, C., Cacchiarelli, D., Grimsby, J., Pokharel, P., Li, S., Morse, M., Lennon, N.J., Livak, K.J., Mikkelsen, T.S., and Rinn, J.L. (2014). The dynamics and regulators of cell fate decisions are revealed by pseudotemporal ordering of single cells. Nat Biotechnol *32*, 381-386.

van der Fits, L., Mourits, S., Voerman, J.S., Kant, M., Boon, L., Laman, J.D., Cornelissen, F., Mus, A.M., Florencia, E., Prens, E.P., and Lubberts, E. (2009). Imiquimod-induced psoriasis-like skin inflammation in mice is mediated via the IL-23/IL-17 axis. J Immunol *182*, 5836-5845.

Wang, Y., Xiao, Y., Li, F., Gu, Y., Yang, M., Zhang, L., Tang, J., and Li, W. (2023). The Clinical Characteristics of Psoriatic Arthritis: A Cross-Sectional Study Based on the Psoriatic Arthritis Cohort of West China Hospital. Rheumatol Ther *10*, 775-784.

Whitley, S.K., Li, M., Kashem, S.W., Hirai, T., Igyarto, B.Z., Knizner, K., Ho, J., Ferris, L.K., Weaver, C.T., Cua, D.J., *et al.* (2022). Local IL-23 is required for proliferation and retention of skin-resident memory T(H)17 cells. Sci Immunol *7*, eabq3254.

Wohn, C., Ober-Blobaum, J.L., Haak, S., Pantelyushin, S., Cheong, C., Zahner, S.P., Onderwater, S., Kant, M., Weighardt, H., Holzmann, B., *et al.* (2013). Langerin(neg) conventional dendritic cells produce IL-23 to drive psoriatic plaque formation in mice. Proc Natl Acad Sci U S A *110*, 10723-10728.

Yang, L., Fan, X., Cui, T., Dang, E., and Wang, G. (2017). Nrf2 Promotes Keratinocyte Proliferation in Psoriasis through Up-Regulation of Keratin 6, Keratin 16, and Keratin 17. J Invest Dermatol *137*, 2168-2176.

Zhang, X., Yin, M., and Zhang, L.J. (2019). Keratin 6, 16 and 17-Critical Barrier Alarmin Molecules in Skin Wounds and Psoriasis. Cells *8*.

Figure 1

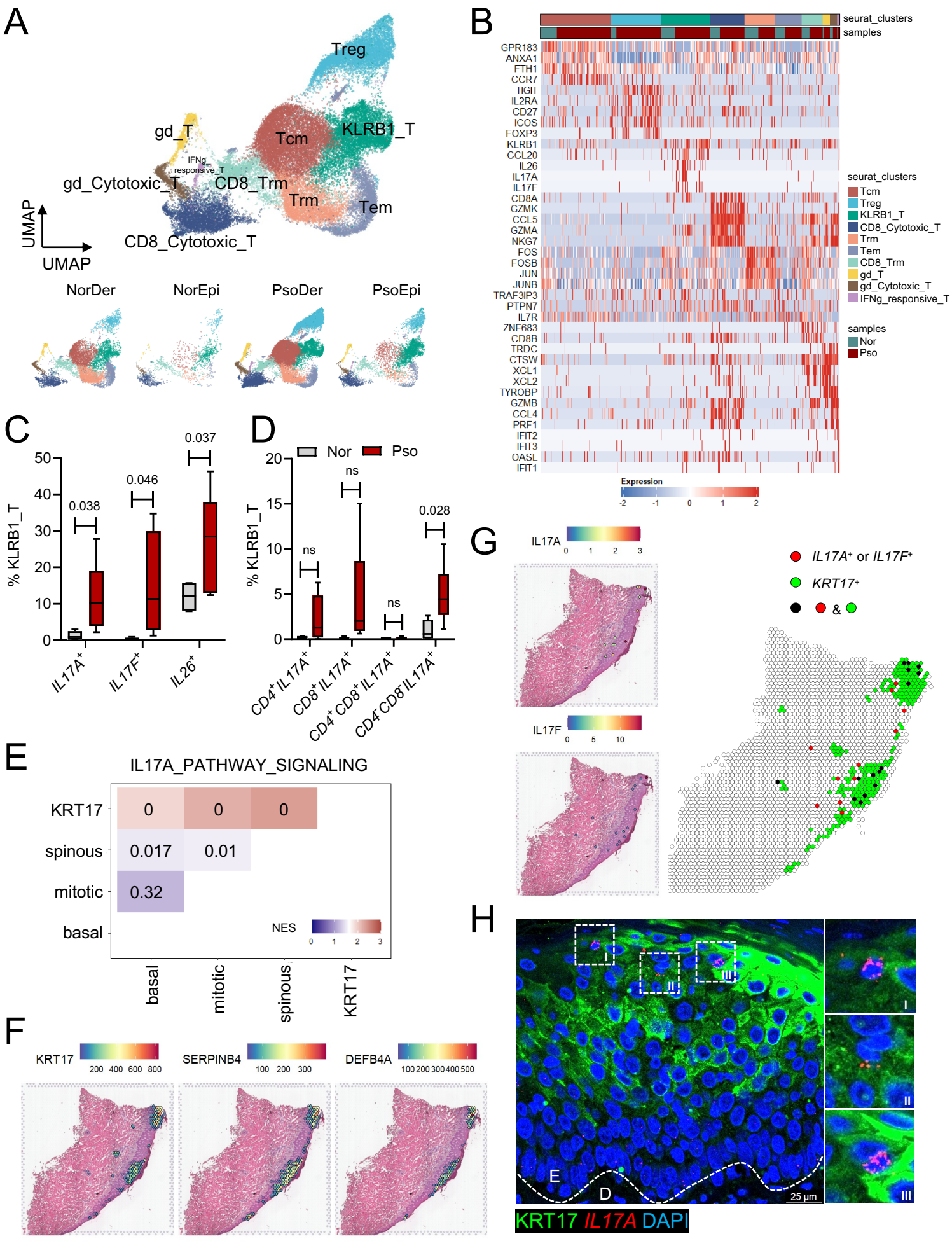
A
Treg
gd_T
Tcm
KLRB1_T
IFNg_responsive_T
gd_Cytotoxic_T
CD8_Trm
Trm
Tem
CD8_Cytotoxic_T
UMAP
UMAP
NorDer
NorEpi
PsoDer
PsoEpi
B
seurat_clusters
samples
GPR183
ANXA1
FTH1
CCR7
TIGIT
IL2RA
CD27
ICOS
FOXP3
KLRB1
CCL20
IL26
IL17A
IL17F
CD8A
GZMK
CCL5
GZMA
NKG7
FOS
FOSB
JUN
JUNB
TRAF3IP3
PTPN7
IL7R
ZNF683
CD8B
TRDC
CTSW
XCL1
XCL2
TYROBP
GZMB
CCL4
PRF1
IFIT2
IFIT3
OASL
IFIT1
Expression
-2 -1 0 1 2
seurat_clusters
Tcm
Treg
KLRB1_T
CD8_Cytotoxic_T
Trm
Tem
CD8_Trm
gd_T
gd_Cytotoxic_T
IFNg_responsive_T
samples
Nor
Pso
C
% KLRB1_T
0.038
0.046
0.037
IL17A+
IL17F+
IL26+
D
Nor
Pso
% KLRB1_T
ns
ns
ns
0.028
CD4+IL17A+
CD8+IL17A+
CD4+CD8+IL17A+
CD4-CD8-IL17A+
E
IL17A_PATHWAY_SIGNALING
KRT17
spinous
mitotic
basal
0
0
0
0.017
0.01
0.32
NES
0 1 2 3
basal
mitotic
spinous
KRT17
F
KRT17
200 400 600 800
SERPINB4
100 200 300
DEFB4A
100 200 300 400 500
G
IL17A
0 1 2 3
IL17F
0 5 10
IL17A+ or IL17F+
KRT17+
&
H
I
II
III
E
D
25 μm
KRT17 IL17A DAPI

Figure 2

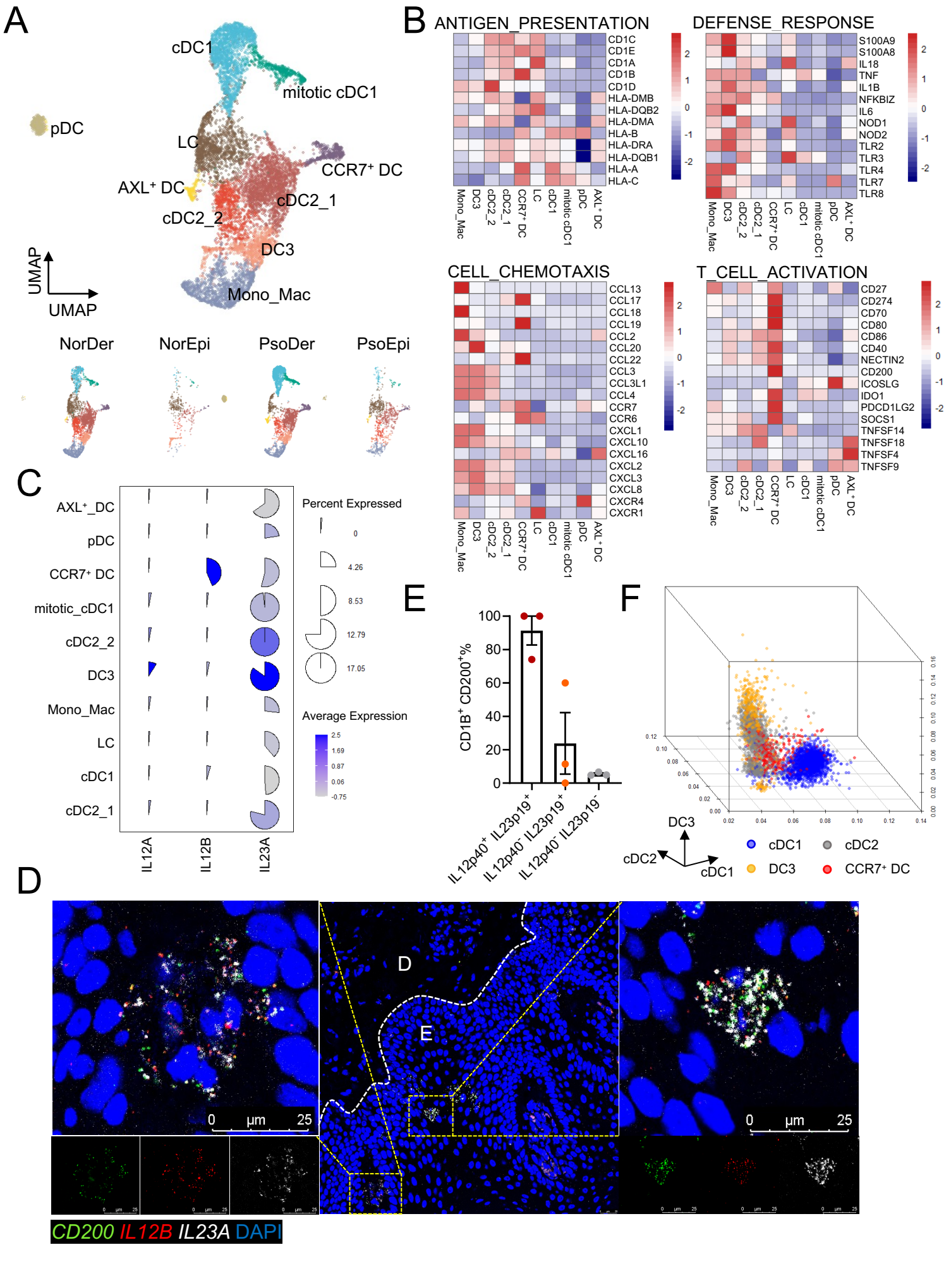
A
cDC1
mitotic cDC1
pDC
LC
CCR7⁺ DC
AXL⁺ DC
cDC2_1
cDC2_2
DC3
Mono_Mac
UMAP
UMAP
NorDer
NorEpi
PsoDer
PsoEpi
B
ANTIGEN_PRESENTATION
CD1C
CD1E
CD1A
CD1B
CD1D
HLA-DMB
HLA-DQB2
HLA-DMA
HLA-B
HLA-DRA
HLA-DQB1
HLA-A
HLA-C
DEFENSE_RESPONSE
S100A9
S100A8
IL18
TNF
IL1B
NFKBIZ
IL6
NOD1
NOD2
TLR2
TLR3
TLR4
TLR7
TLR8
CELL_CHEMOTAXIS
CCL13
CCL17
CCL18
CCL19
CCL2
CCL20
CCL22
CCL3
CCL3L1
CCL4
CCR7
CCR6
CXCL1
CXCL10
CXCL16
CXCL2
CXCL3
CXCL8
CXCR4
CXCR1
T_CELL_ACTIVATION
CD27
CD274
CD70
CD80
CD86
CD40
NECTIN2
CD200
ICOSLG
IDO1
PDCD1LG2
SOCS1
TNFSF14
TNFSF18
TNFSF4
TNFSF9
Mono_Mac
DC3
cDC2_2
cDC2_1
CCR7⁺ DC
LC
cDC1
mitotic cDC1
pDC
AXL⁺ DC
C
AXL⁺_DC
pDC
CCR7⁺ DC
mitotic_cDC1
cDC2_2
DC3
Mono_Mac
LC
cDC1
cDC2_1
IL12A
IL12B
IL23A
Percent Expressed
0
4.26
8.53
12.79
17.05
Average Expression
2.5
1.69
0.87
0.06
-0.75
E
CD1B⁺ CD200⁺ %
IL12p40⁺ IL23p19⁺
IL12p40⁻ IL23p19⁺
IL12p40⁻ IL23p19⁻
F
DC3
cDC2
cDC1
cDC1
DC3
CCR7⁺ DC
D
D
E
0 µm 25
0 µm 25
CD200 IL12B IL23A DAPI

Figure 3

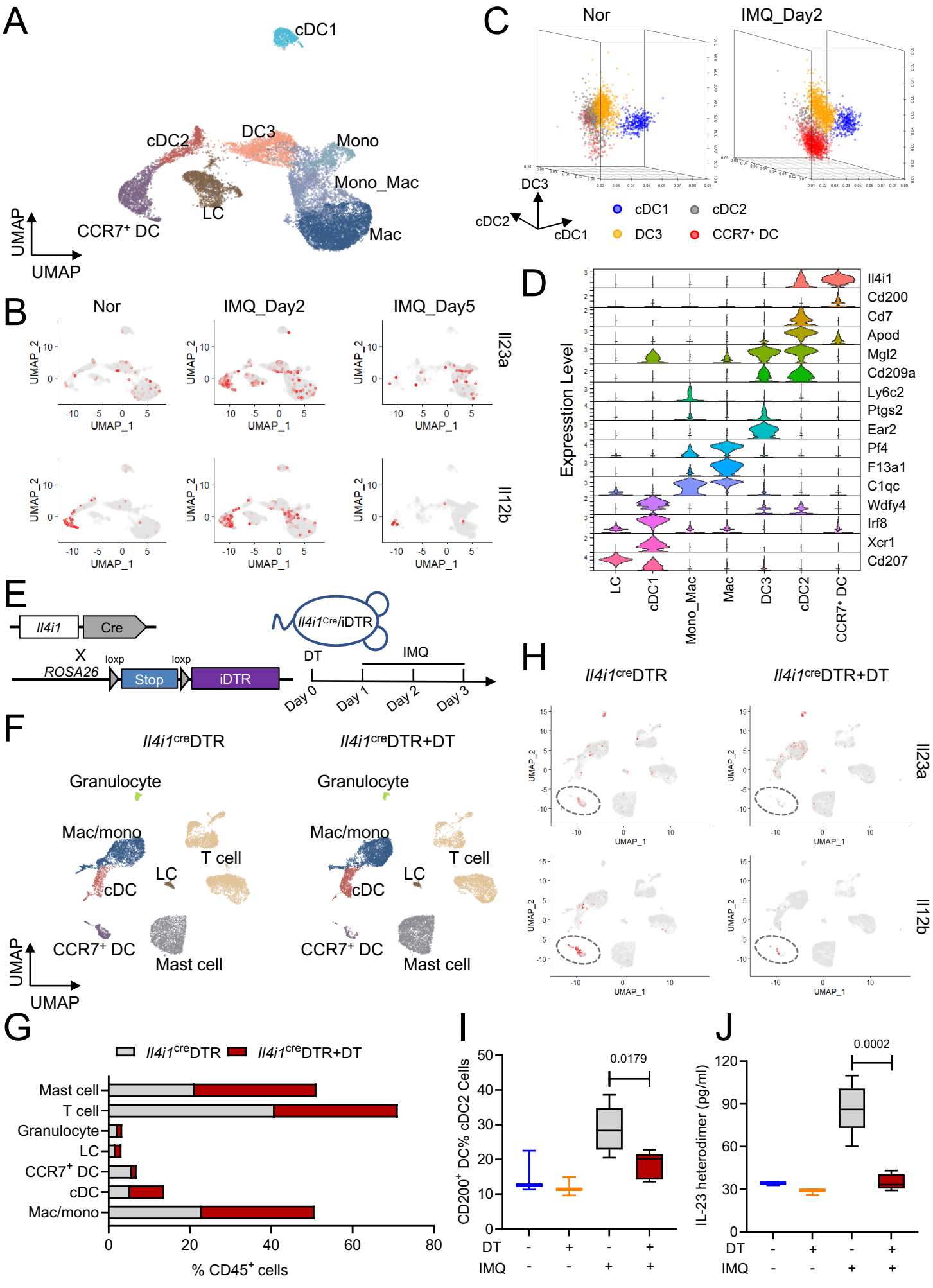
A
cDC1
cDC2
DC3
Mono
Mono_Mac
LC
CCR7⁺ DC
Mac
UMAP
UMAP
B
Nor
IMQ_Day2
IMQ_Day5
Il23a
Il12b
UMAP_1
UMAP_2
C
Nor
IMQ_Day2
DC3
cDC2
cDC1
cDC1
cDC2
DC3
CCR7⁺ DC
D
Expression Level
Il4i1
Cd200
Cd7
Apod
Mgl2
Cd209a
Ly6c2
Ptgs2
Ear2
Pf4
F13a1
C1qc
Wdfy4
Irf8
Xcr1
Cd207
LC
cDC1
Mono_Mac
Mac
DC3
cDC2
CCR7⁺ DC
E
Il4i1
Cre
X
ROSA26
loxp
Stop
loxp
iDTR
Il4i1Cre/iDTR
DT
IMQ
Day 0
Day 1
Day 2
Day 3
F
Il4i1creDTR
Il4i1creDTR+DT
Granulocyte
Mac/mono
T cell
LC
cDC
CCR7⁺ DC
Mast cell
UMAP
UMAP
G
Il4i1creDTR
Il4i1creDTR+DT
Mast cell
T cell
Granulocyte
LC
CCR7⁺ DC
cDC
Mac/mono
0
20
40
60
80
% CD45⁺ cells
H
Il4i1creDTR
Il4i1creDTR+DT
Il23a
Il12b
UMAP_1
UMAP_2
I
CD200⁺ DC% cDC2 Cells
0.0179
DT
IMQ
J
IL-23 heterodimer (pg/ml)
0.0002
DT
IMQ

Figure 4

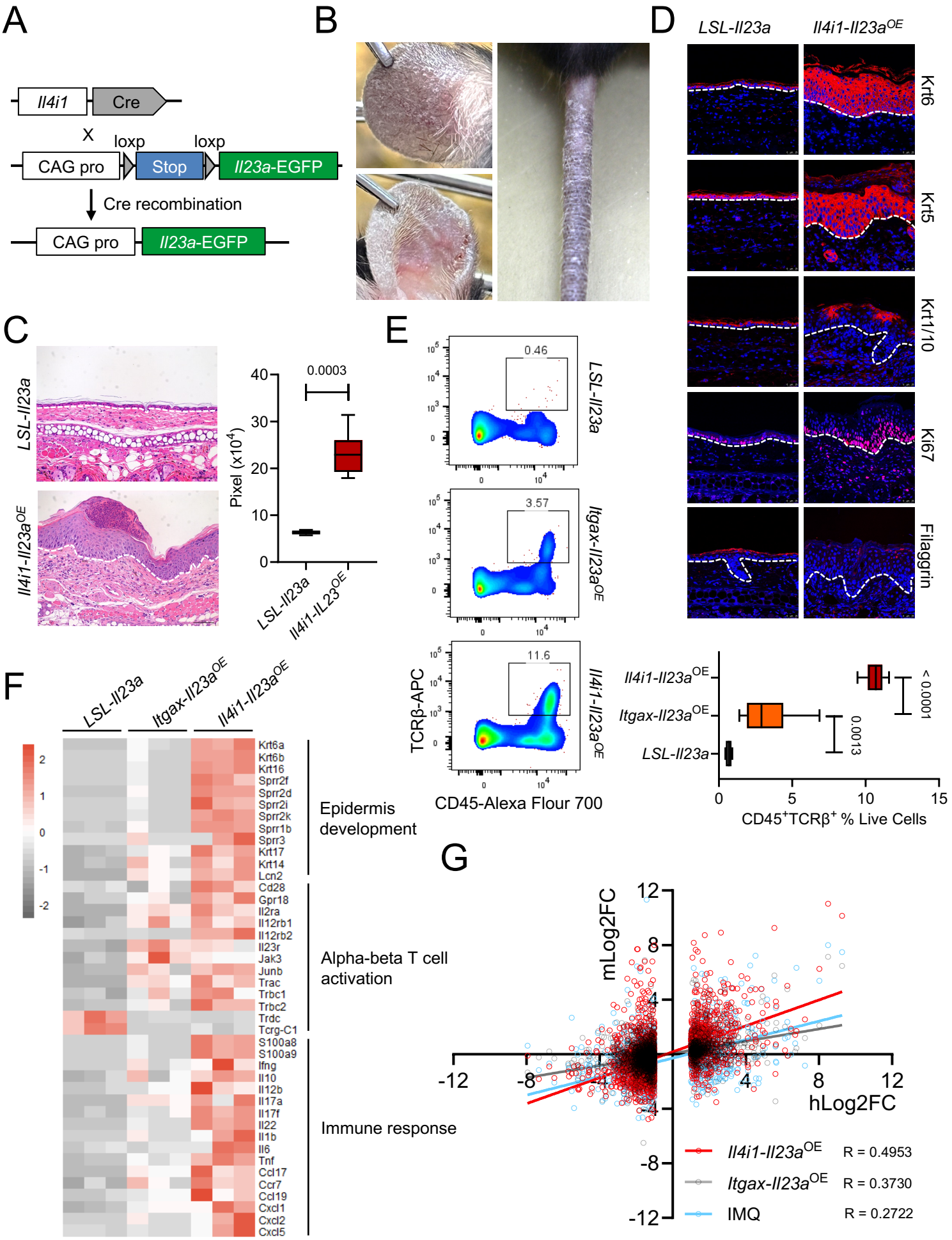
A
Il4i1
Cre
X
loxp
loxp
CAG pro
Stop
Il23a-EGFP
Cre recombination
CAG pro
Il23a-EGFP
B
C
LSL-Il23a
Il4i1-Il23a^OE
0.0003
Pixel (x10^4)
LSL-Il23a
Il4i1-IL23^OE
D
LSL-Il23a
Il4i1-Il23a^OE
Krt6
Krt5
Krt1/10
Ki67
Filaggrin
E
0.46
3.57
11.6
LSL-Il23a
Itgax-Il23a^OE
Il4i1-Il23a^OE
TCRβ-APC
CD45-Alexa Flour 700
Il4i1-Il23a^OE
Itgax-Il23a^OE
LSL-Il23a
0.0013
< 0.0001
CD45+TCRβ+ % Live Cells
F
LSL-Il23a
Itgax-Il23a^OE
Il4i1-Il23a^OE
Krt6a
Krt6b
Krt16
Sprr2f
Sprr2d
Sprr2i
Sprr2k
Sprr1b
Sprr3
Krt17
Krt14
Lcn2
Cd28
Gpr18
Il2ra
Il12rb1
Il12rb2
Il23r
Jak3
Junb
Trac
Trbc1
Trbc2
Trdc
Tcrg-C1
S100a8
S100a9
Ifng
Il10
Il12b
Il17a
Il17f
Il22
Il1b
Il6
Tnf
Ccl17
Ccr7
Ccl19
Cxcl1
Cxcl2
Cxcl5
Epidermis development
Alpha-beta T cell activation
Immune response
G
mLog2FC
hLog2FC
Il4i1-Il23a^OE
R = 0.4953
Itgax-Il23a^OE
R = 0.3730
IMQ
R = 0.2722

Figure 5

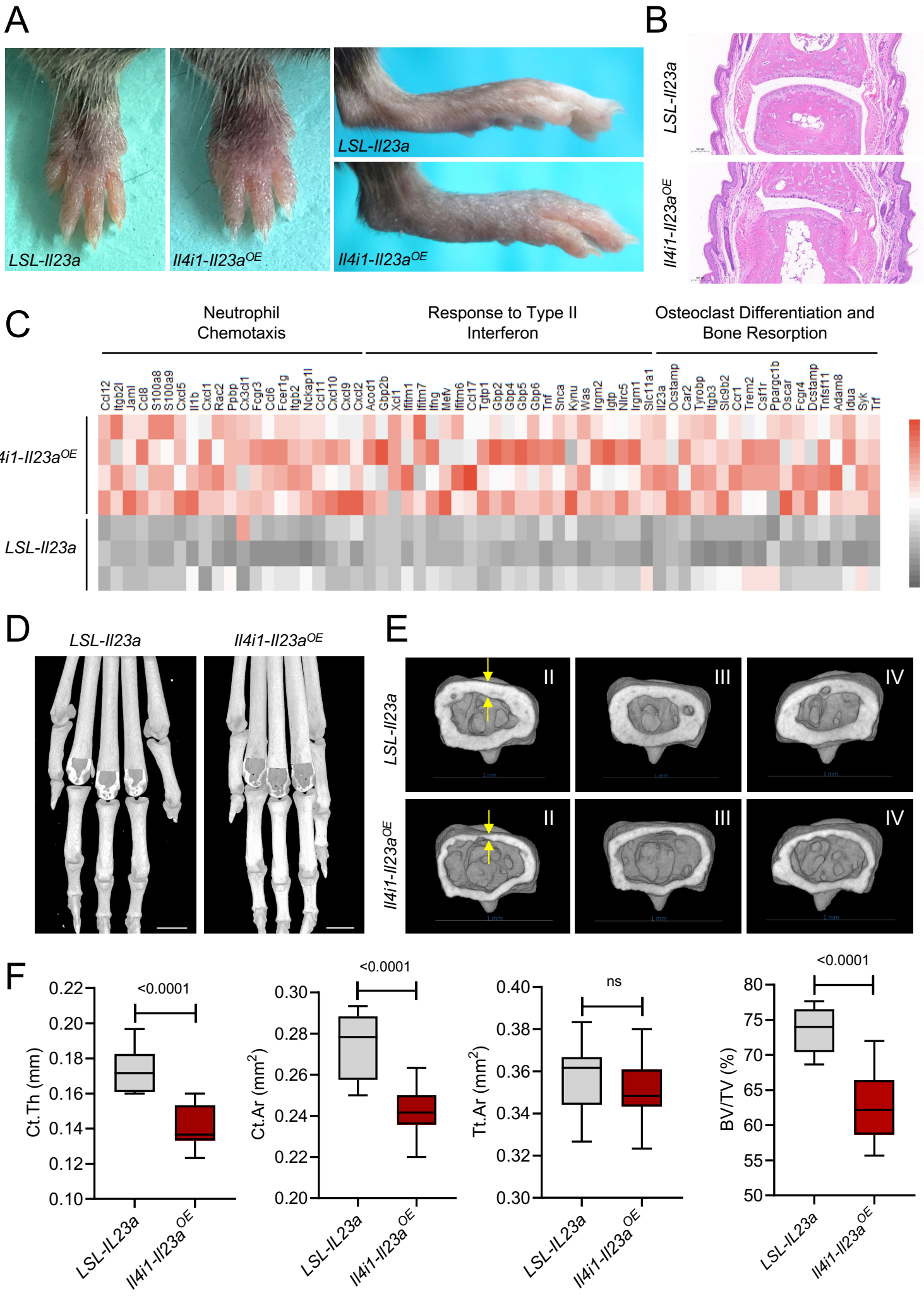
A
LSL-Il23a
Il4i1-Il23a^OE
LSL-Il23a
Il4i1-Il23a^OE
B
LSL-Il23a
Il4i1-Il23a^OE
C
Neutrophil Chemotaxis
Response to Type II Interferon
Osteoclast Differentiation and Bone Resorption
Ccl12 Itgb2l Jaml Ccl8 S100a8 S100a9 Cxcl5 Il1b Cxcl1 Rac2 Ppbp Cx3cl1 Fcgr3 Ccl6 Fcer1g Itgb2 Nckap1l Ccl11 Cxcl10 Cxcl9 Cxcl2 Acod1 Gbp2b Xcl1 Ifittm1 Ifitm7 Ifng Mefv Ifitm6 Ccl17 Tgtp1 Gbp2 Gbp4 Gbp5 Gbp6 Tnf Snca Kynu Was Irgm2 Igtp Nlrc5 Irgm1 Slc11a1 Il23a Ocstamp Car2 Tyrobp Itgb3 Slc9b2 Ccr1 Trem2 Csf1r Ppargc1b Oscar Fcgr4 Dcstamp Tnfsf11 Adam8 Idua Syk Trf
Il4i1-Il23a^OE
LSL-Il23a
2
1
0
-1
-2
D
LSL-Il23a
Il4i1-Il23a^OE
E
LSL-Il23a
Il4i1-Il23a^OE
II
III
IV
F
Ct.Th (mm)
<0.0001
Ct.Ar (mm²)
<0.0001
Tt.Ar (mm²)
ns
BV/TV (%)
<0.0001
LSL-IL23a
Il4i1-Il23a OE

Figure 6

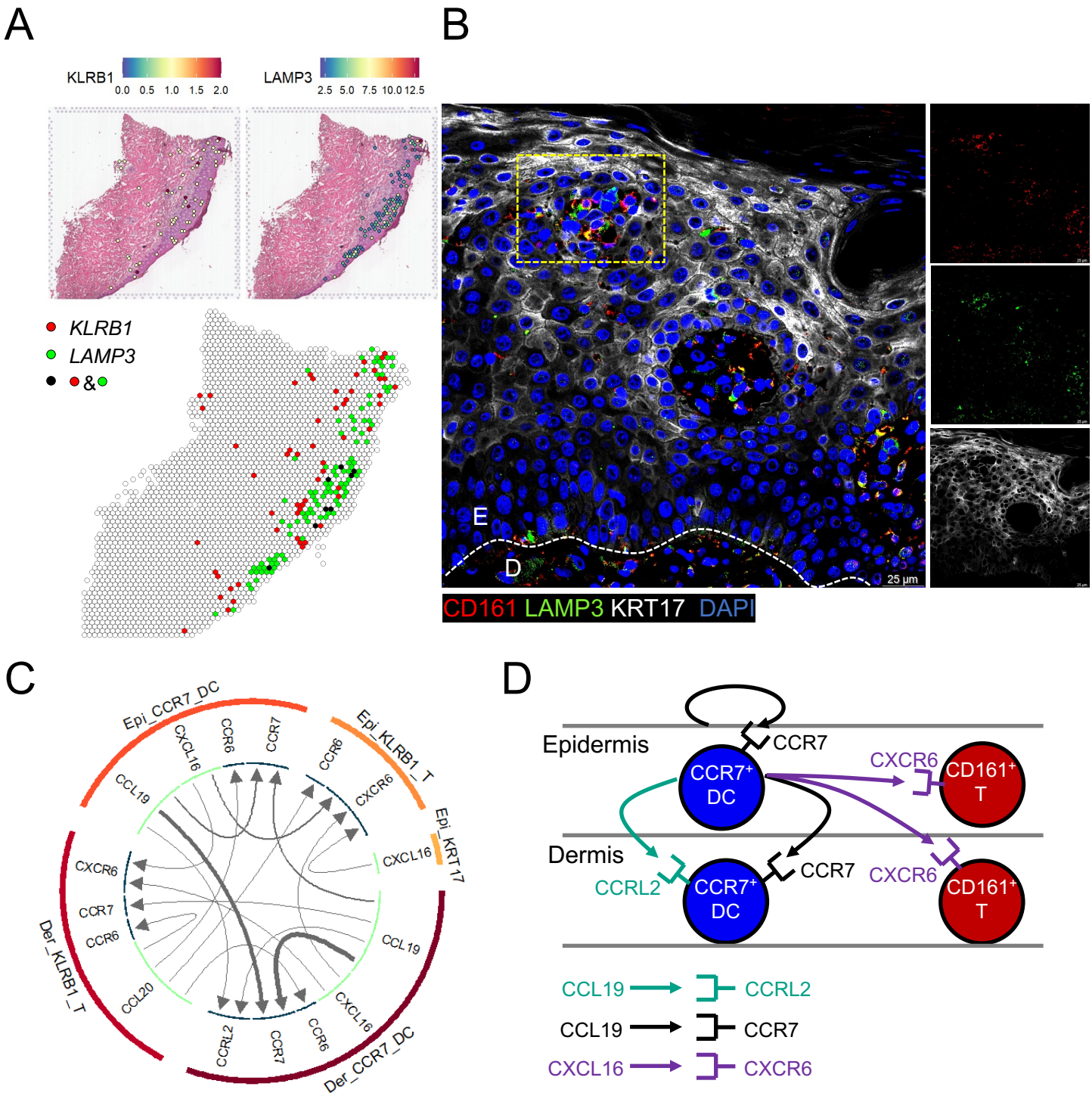
A
KLRB1
0.0 0.5 1.0 1.5 2.0
LAMP3
2.5 5.0 7.5 10.0 12.5
KLRB1
LAMP3
&
B
E
D
25 µm
CD161 LAMP3 KRT17 DAPI
C
Epi_CCR7_DC
Epi_KLRB1_T
Epi_KRT17
Der_KLRB1_T
Der_CCR7_DC
CXCL16
CCR6
CCR7
CXCR6
CCL19
CCL20
CCRL2
D
Epidermis
Dermis
CCR7+ DC
CCR7
CXCR6
CD161+ T
CCRL2
CCL19 → CCRL2
CCL19 → CCR7
CXCL16 → CXCR6

Figure S1

A

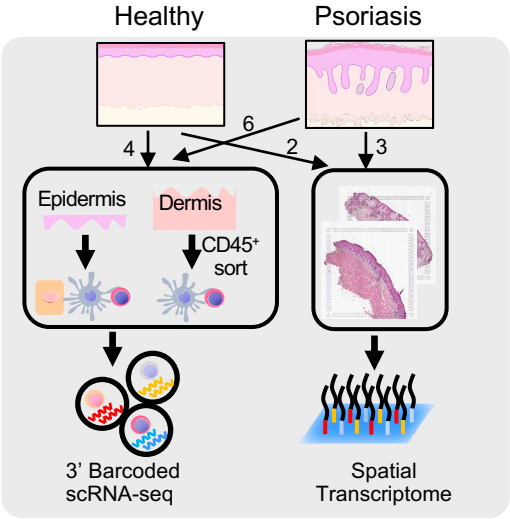

B

Assay	3'		Spatial	
Group	Nor (n = 4)	Pso (n = 6)	Nor (n = 2)	Pso (n = 3)
Age	25-55	27-59	27-32	32-65
Anatomic site	trunk, limbs, eyelid	trunk, limbs	trunk, scalp	trunk
Type	NA	vulgaris	NA	vulgaris
Topical score	NA	5-10	NA	8-10
Duration of disease	NA	1 month-5 years	NA	3 weeks-5 years
Treatment	Not treated or washed-out for ≥ 6 months prior to the research biopsy			

C

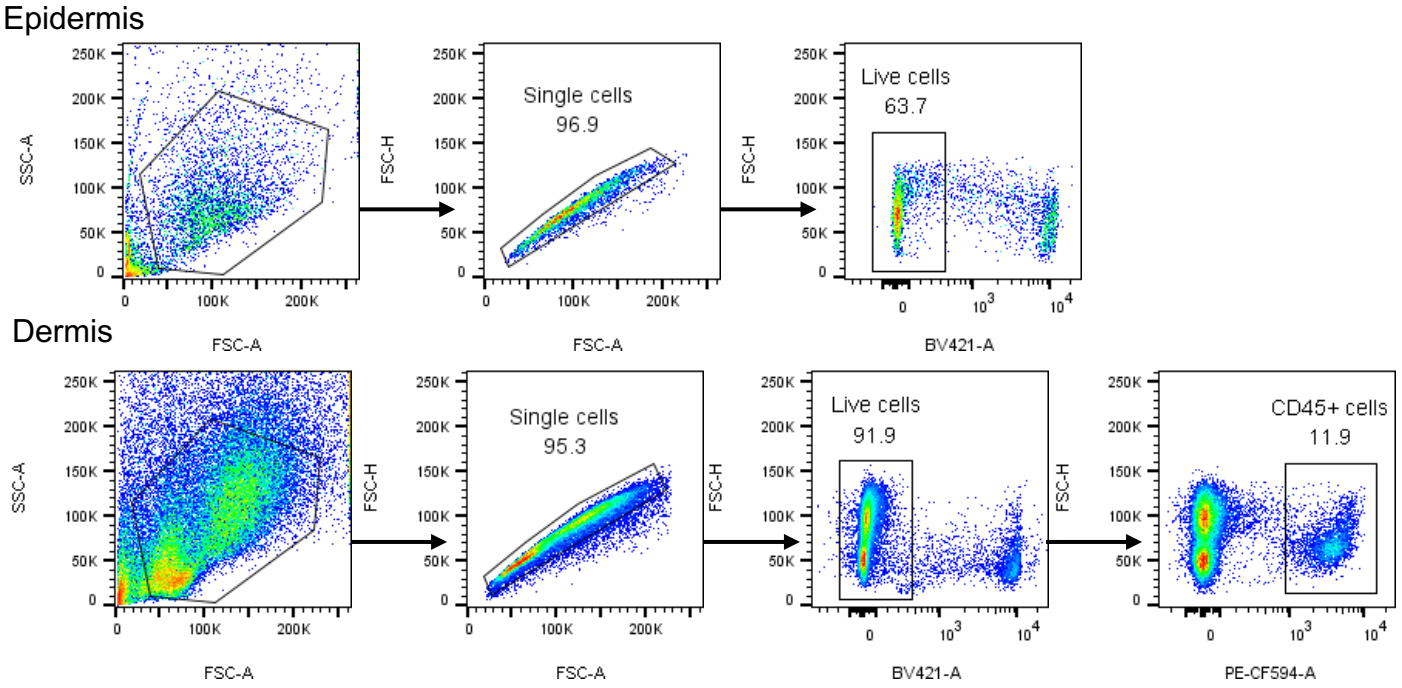

D

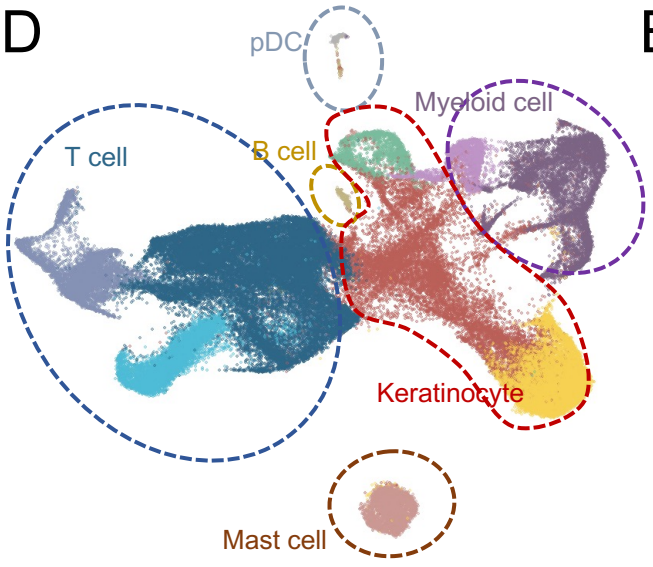

E

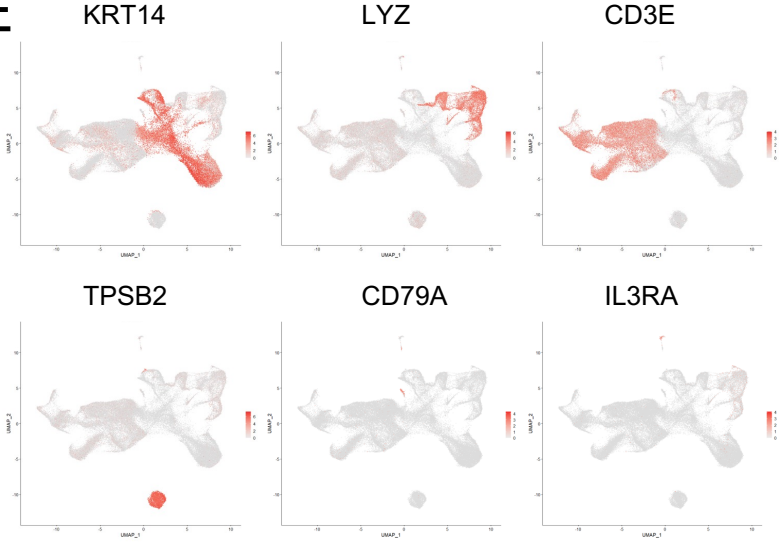

Figure S2

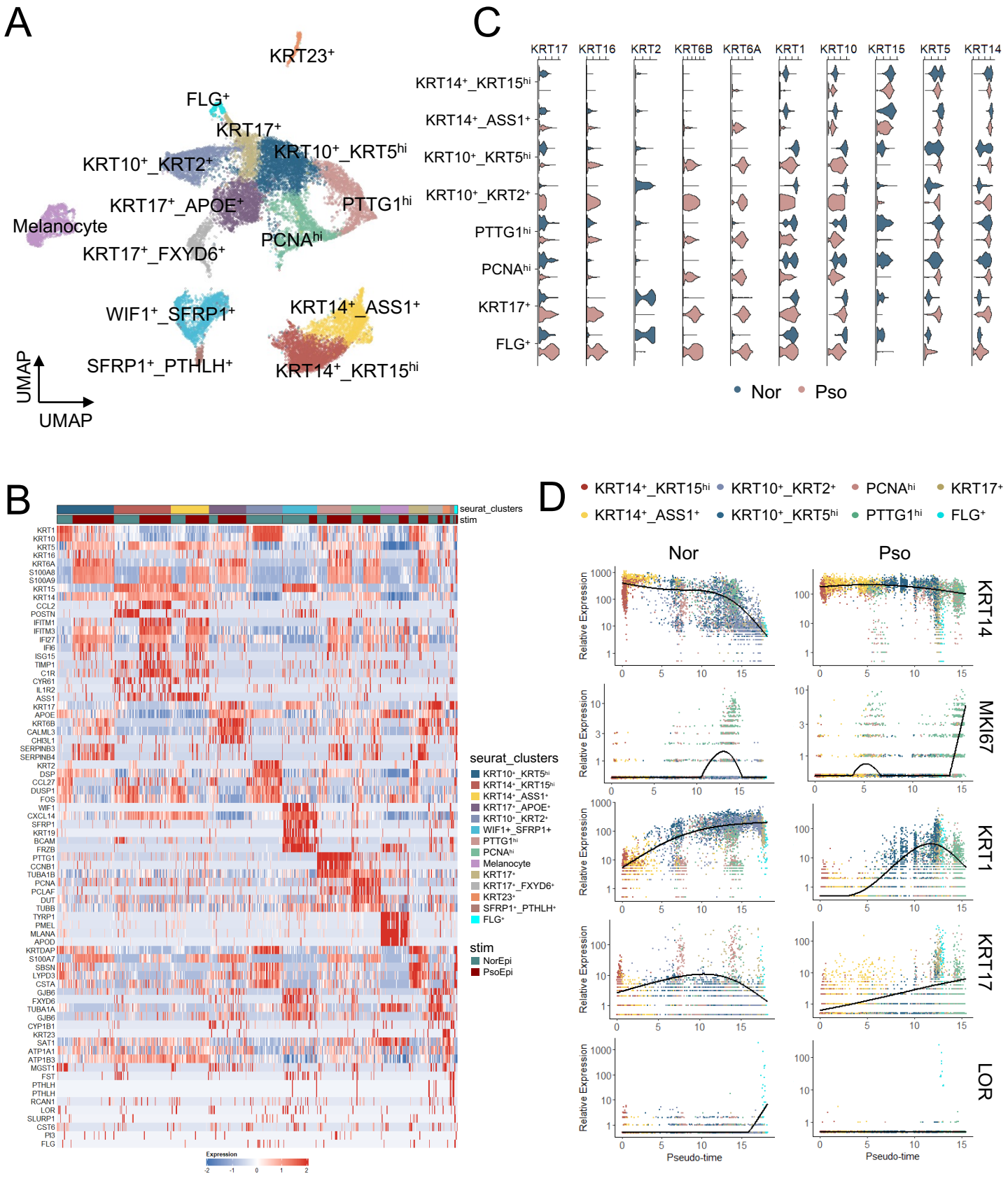
A
KRT23+
FLG+
KRT17+
KRT10+_KRT5hi
KRT10+_KRT2+
KRT17+_APOE+
PTTG1hi
Melanocyte
PCNAhi
KRT17+_FXYD6+
WIF1+_SFRP1+
KRT14+_ASS1+
SFRP1+_PTHLH+
KRT14+_KRT15hi
UMAP
UMAP
C
KRT17
KRT16
KRT2
KRT6B
KRT6A
KRT1
KRT10
KRT15
KRT5
KRT14
KRT14+_KRT15hi
KRT14+_ASS1+
KRT10+_KRT5hi
KRT10+_KRT2+
PTTG1hi
PCNAhi
KRT17+
FLG+
Nor
Pso
B
seurat_clusters
stim
KRT1
KRT10
KRT5
KRT16
KRT6A
S100A8
S100A9
KRT15
KRT14
CCL2
POSTN
IFITM1
IFITM3
IFI27
IF6
ISG15
TIMP1
C1R
CYR61
IL1R2
ASS1
KRT17
APOE
KRT6B
CALML3
CHI3L1
SERPINB3
SERPINB4
KRT2
DSP
CCL27
DUSP1
FOS
WIF1
CXCL14
SFRP1
KRT19
BCAM
FRZB
PTTG1
CCNB1
TUBA1B
PCNA
PCLAF
DUT
TUBB
TYRP1
PMEL
MLANA
APOD
KRTDAP
S100A7
SBSN
LYPD3
CSTA
GJB6
FXYD6
TUBA1A
GJB6
CYP1B1
KRT23
SAT1
ATP1A1
ATP1B3
MGST1
FST
PTHLH
PTHLH
RCAN1
LOR
SLURP1
CST6
PI3
FLG
Expression
-2
-1
0
1
2
seurat_clusters
KRT10+_KRT5hi
KRT14+_KRT15hi
KRT14+_ASS1+
KRT17+_APOE+
KRT10+_KRT2+
WIF1+_SFRP1+
PTTG1hi
PCNAhi
Melanocyte
KRT17+
KRT17+_FXYD6+
KRT23+
SFRP1+_PTHLH+
FLG+
stim
NorEpi
PsoEpi
D
KRT14+_KRT15hi
KRT10+_KRT2+
PCNAhi
KRT17+
KRT14+_ASS1+
KRT10+_KRT5hi
PTTG1hi
FLG+
Nor
Pso
Relative Expression
KRT14
MKI67
KRT1
KRT17
LOR
Pseudo-time
Pseudo-time

Figure S3

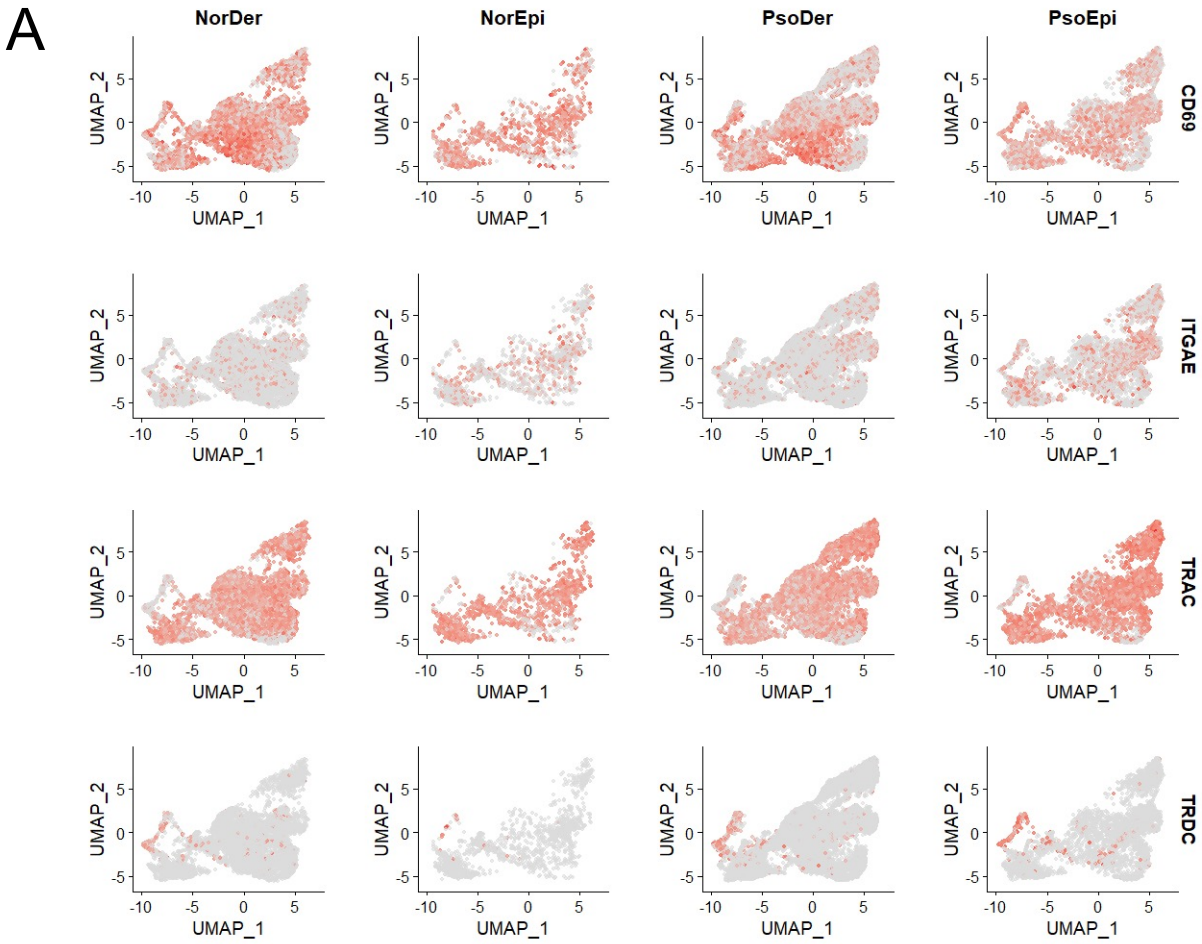
A
NorDer
NorEpi
PsoDer
PsoEpi
CD69
ITGAE
TRAC
TRDC
UMAP_1
UMAP_2

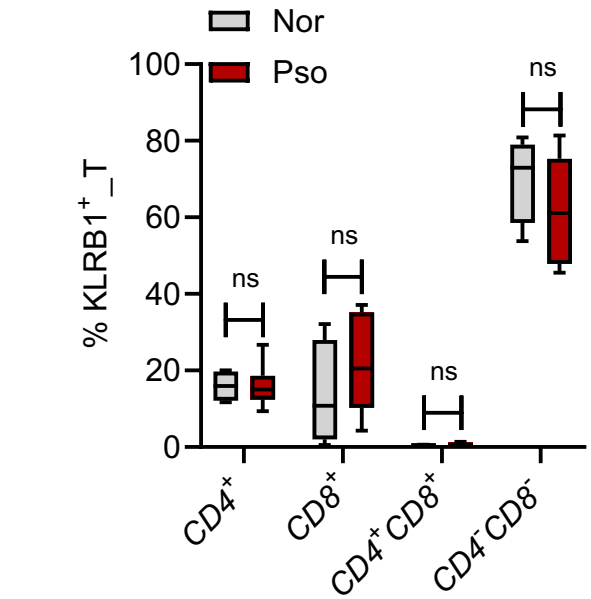
B
Nor
Pso
% KLRB1+ _T
ns
CD4+
CD8+
CD4+CD8+
CD4-CD8-

Figure S4

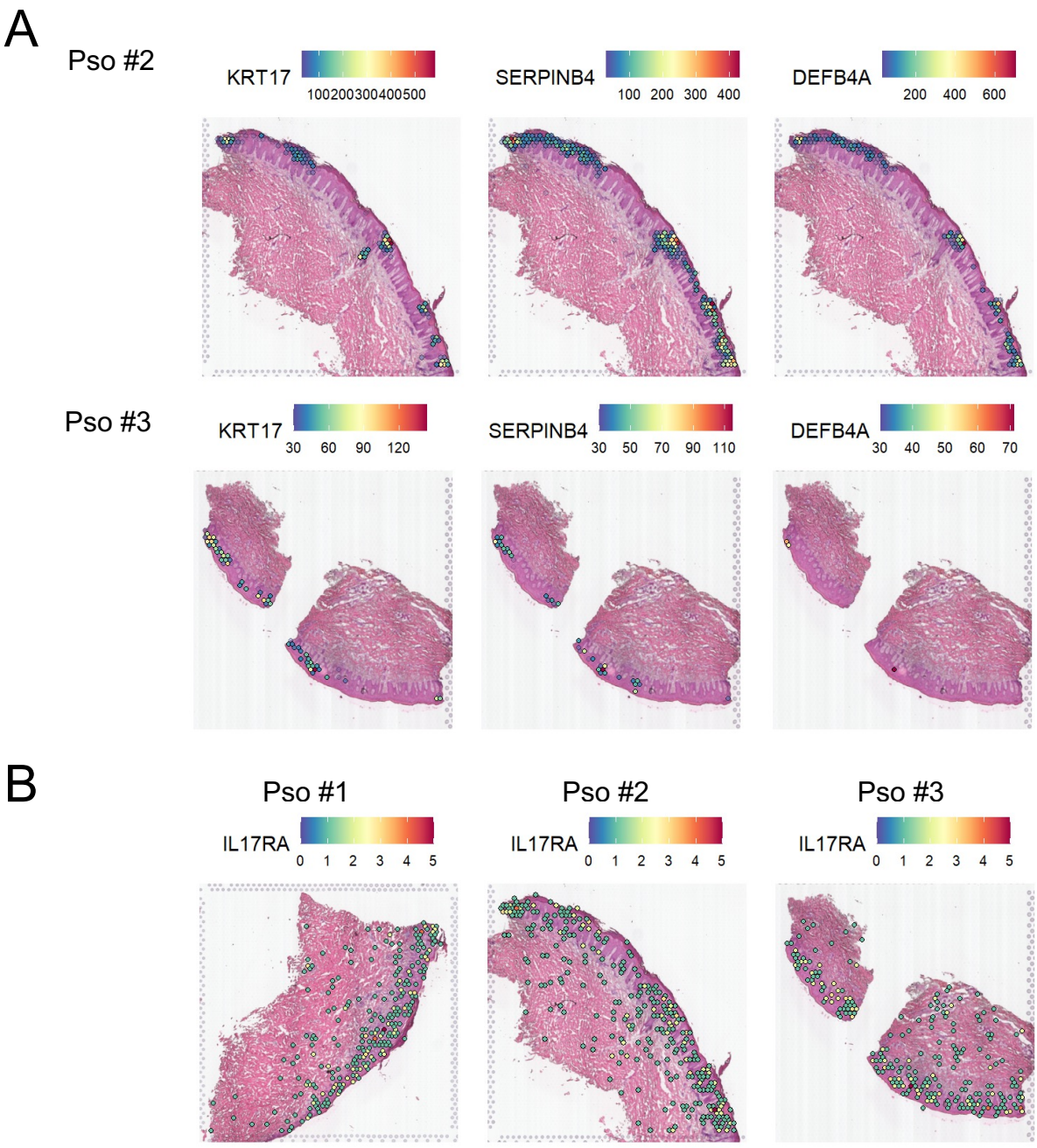
A
Pso #2
KRT17
100200300400500
SERPINB4
100 200 300 400
DEFB4A
200 400 600
Pso #3
KRT17
30 60 90 120
SERPINB4
30 50 70 90 110
DEFB4A
30 40 50 60 70
B
Pso #1
IL17RA
0 1 2 3 4 5
Pso #2
IL17RA
0 1 2 3 4 5
Pso #3
IL17RA
0 1 2 3 4 5
C
Nor
Pso
100 μm
KRT17 IL17RA DAPI

Figure S5

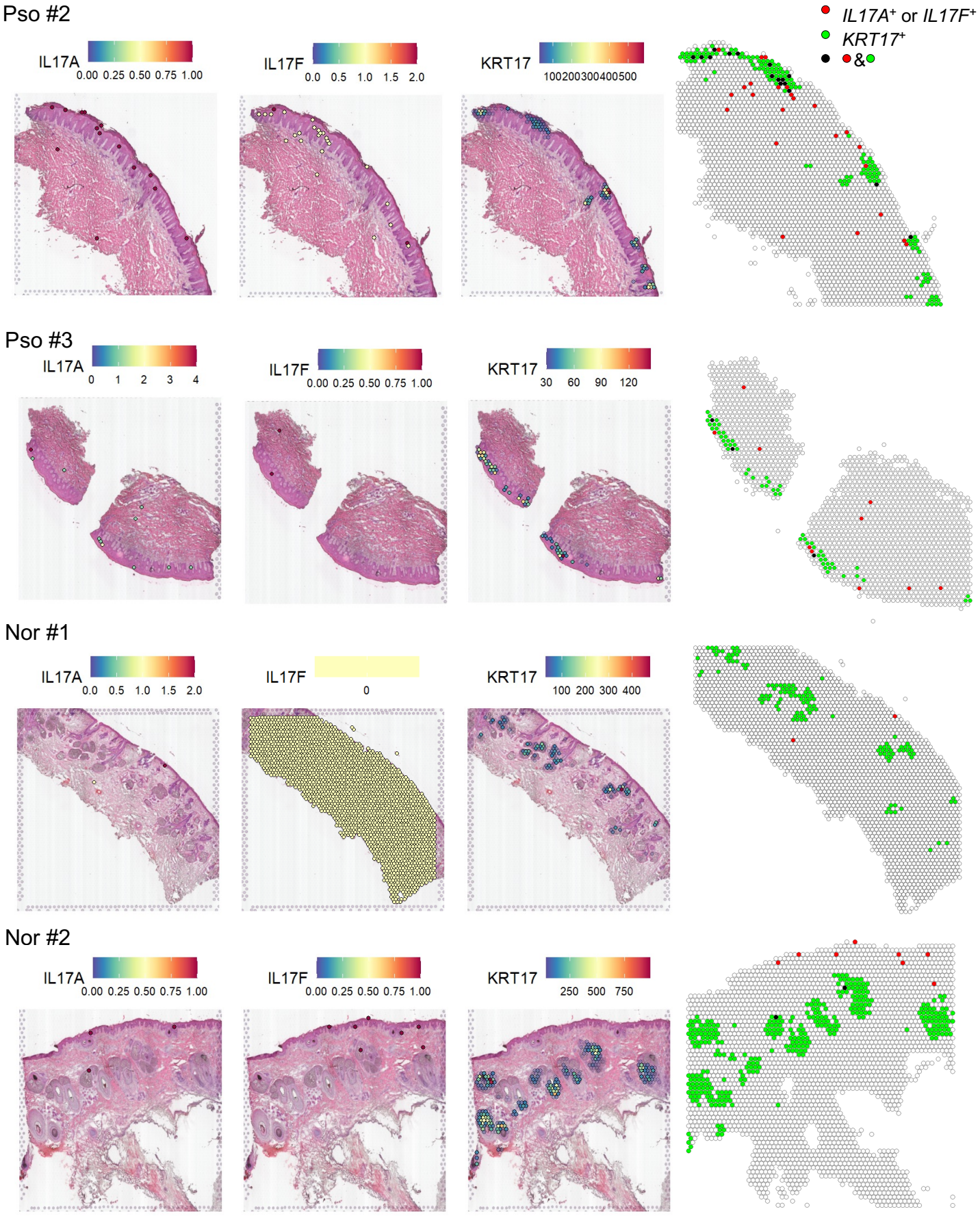
Pso #2
IL17A
0.00 0.25 0.50 0.75 1.00
IL17F
0.0 0.5 1.0 1.5 2.0
KRT17
100200300400500
IL17A+ or IL17F+
KRT17+
&
Pso #3
IL17A
0 1 2 3 4
IL17F
0.00 0.25 0.50 0.75 1.00
KRT17
30 60 90 120
Nor #1
IL17A
0.0 0.5 1.0 1.5 2.0
IL17F
0
KRT17
100 200 300 400
Nor #2
IL17A
0.00 0.25 0.50 0.75 1.00
IL17F
0.00 0.25 0.50 0.75 1.00
KRT17
250 500 750

Figure S6

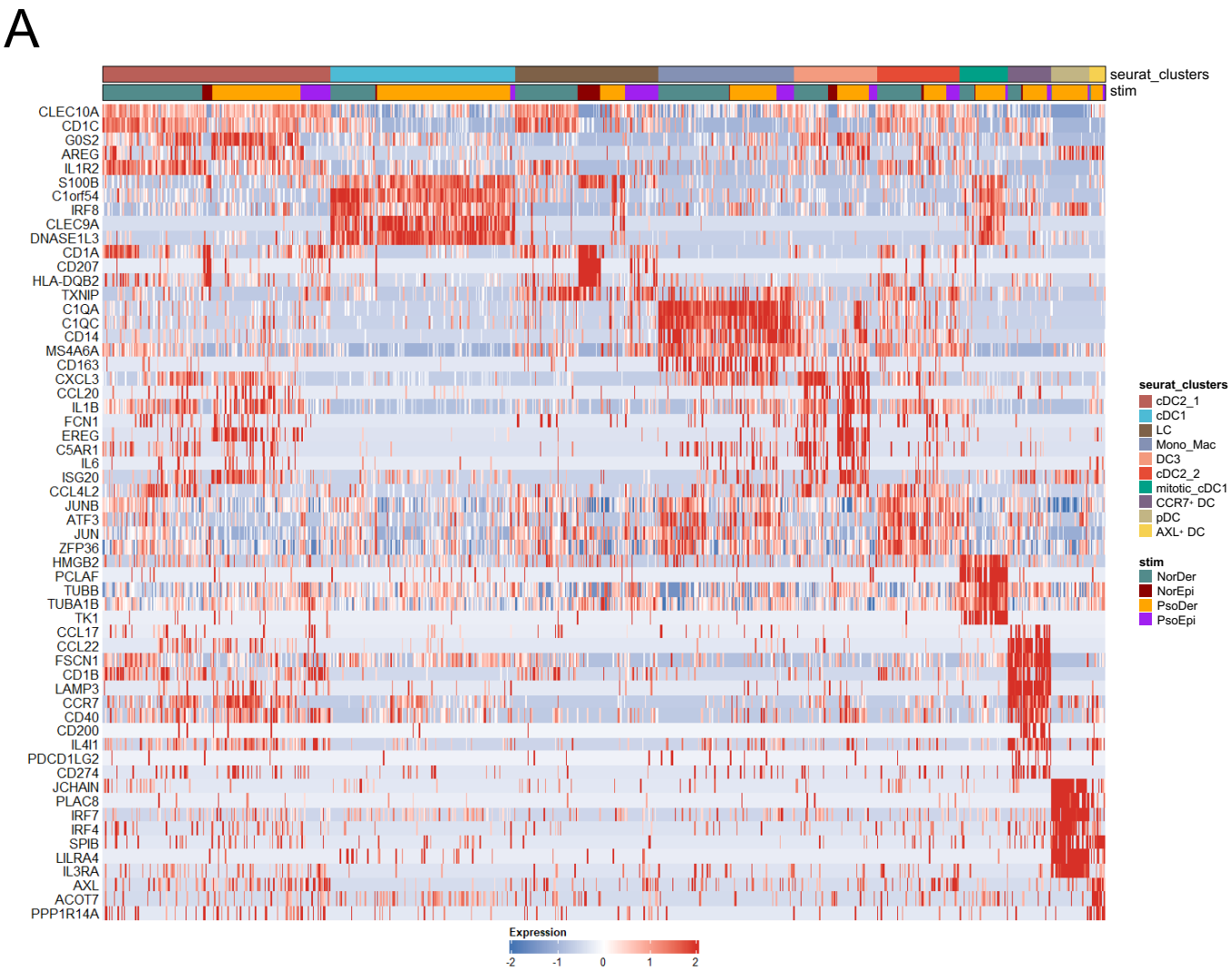
A
seurat_clusters
stim
CLEC10A
CD1C
G0S2
AREG
IL1R2
S100B
C1orf54
IRF8
CLEC9A
DNASE1L3
CD1A
CD207
HLA-DQB2
TXNIP
C1QA
C1QC
CD14
MS4A6A
CD163
CXCL3
CCL20
IL1B
FCN1
EREG
C5AR1
IL6
ISG20
CCL4L2
JUNB
ATF3
JUN
ZFP36
HMGB2
PCLAF
TUBB
TUBA1B
TK1
CCL17
CCL22
FSCN1
CD1B
LAMP3
CCR7
CD40
CD200
IL4I1
PDCD1LG2
CD274
JCHAIN
PLAC8
IRF7
IRF4
SPIB
LILRA4
IL3RA
AXL
ACOT7
PPP1R14A
seurat_clusters
cDC2_1
cDC1
LC
Mono_Mac
DC3
cDC2_2
mitotic_cDC1
CCR7+ DC
pDC
AXL+ DC
stim
NorDer
NorEpi
PsoDer
PsoEpi
Expression
-2
-1
0
1
2

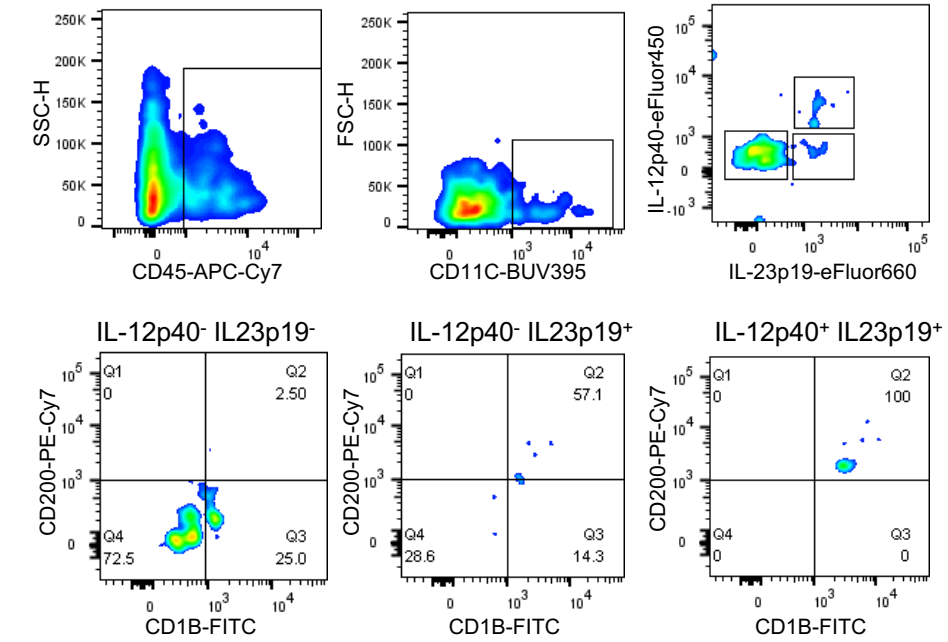
B
SSC-H
CD45-APC-Cy7
FSC-H
CD11C-BUV395
IL-12p40-eFluor450
IL-23p19-eFluor660
IL-12p40- IL23p19-
IL-12p40- IL23p19+
IL-12p40+ IL23p19+
CD200-PE-Cy7
CD1B-FITC
Q1
Q2
Q3
Q4
0
2.50
72.5
25.0
57.1
28.6
14.3
100

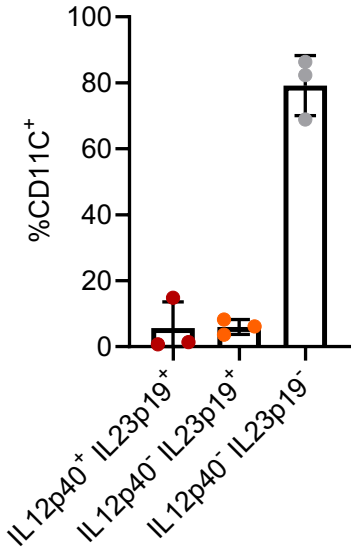
C
%CD11C+
IL12p40+ IL23p19+
IL12p40- IL23p19+
IL12p40- IL23p19-

Figure S7

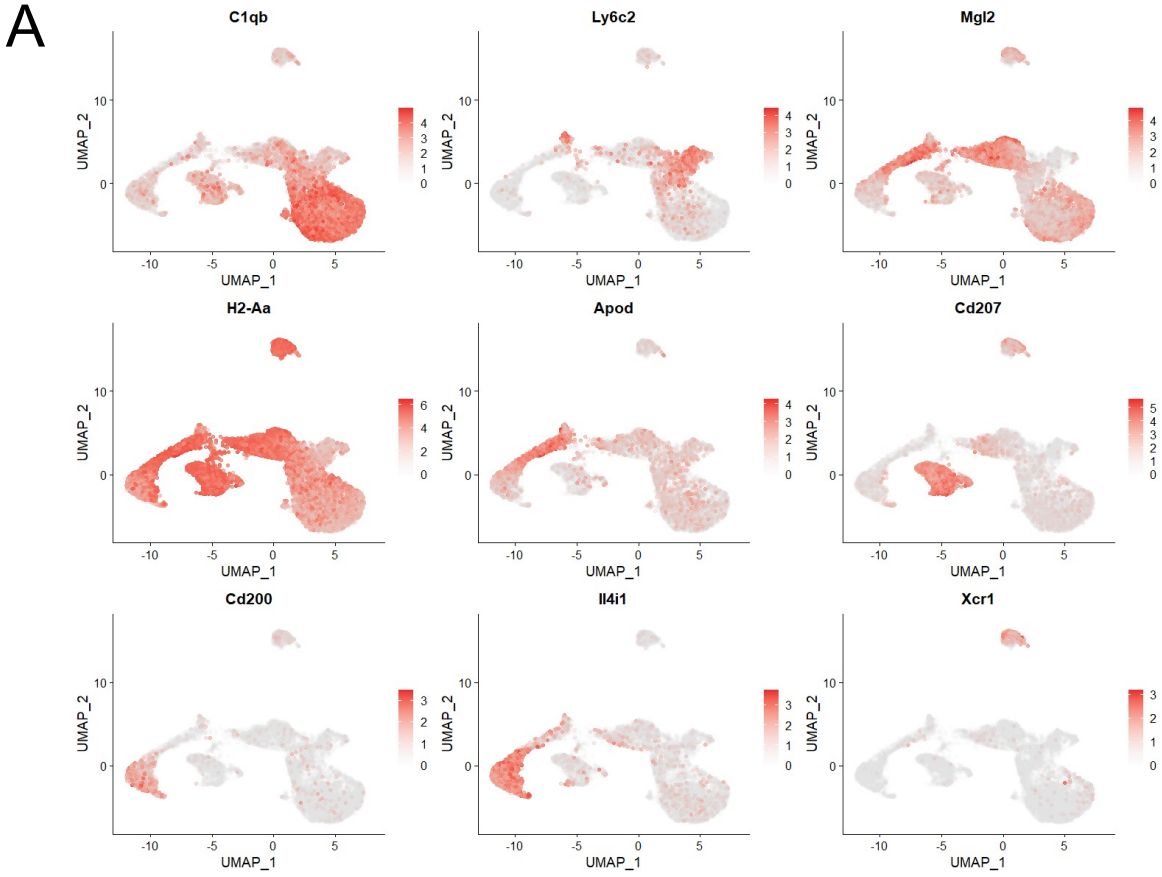
A
C1qb
Ly6c2
Mgl2
H2-Aa
Apod
Cd207
Cd200
Il4i1
Xcr1
UMAP_1
UMAP_2

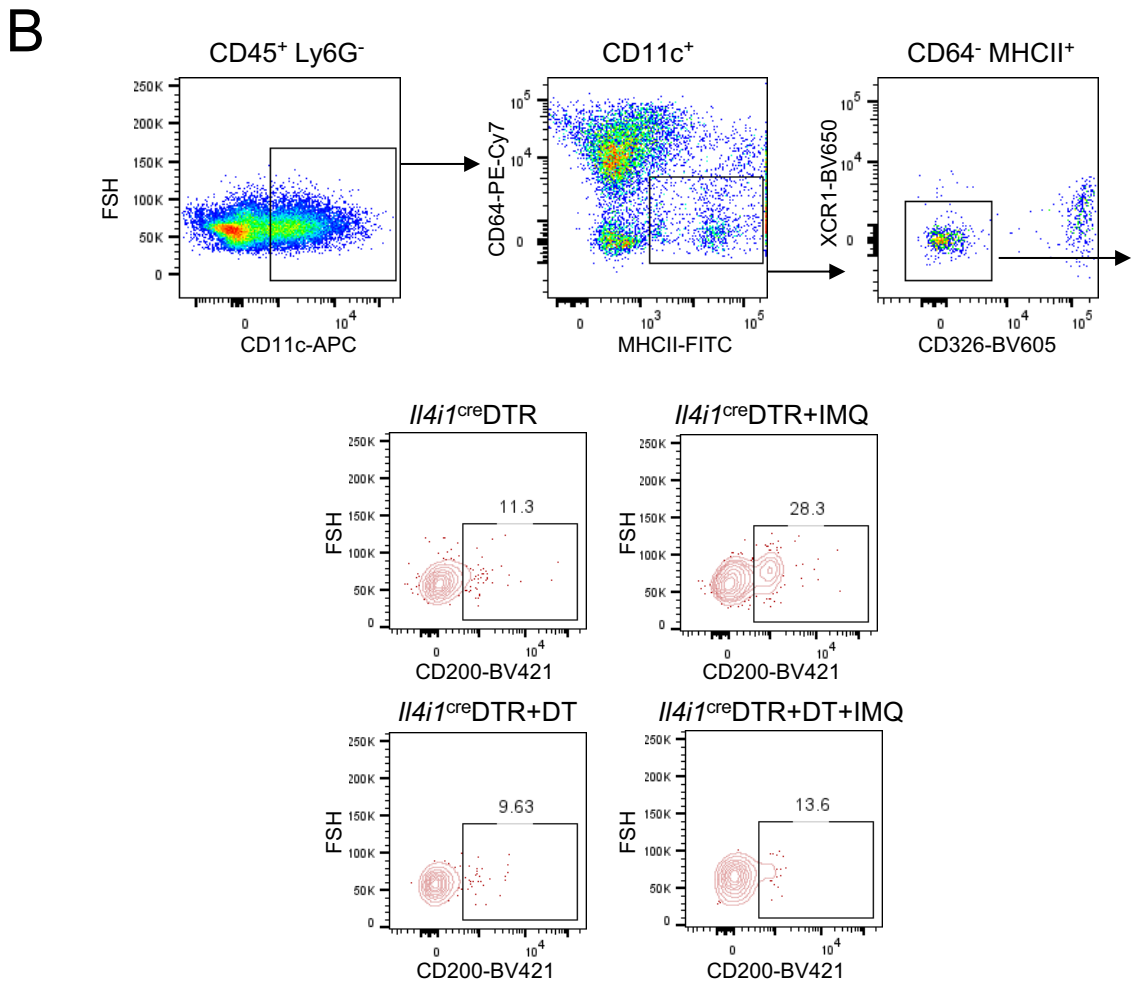
B
CD45+ Ly6G-
CD11c+
CD64- MHCII+
FSH
CD11c-APC
CD64-PE-Cy7
MHCII-FITC
XCR1-BV650
CD326-BV605
Il4i1creDTR
Il4i1creDTR+IMQ
Il4i1creDTR+DT
Il4i1creDTR+DT+IMQ
11.3
28.3
9.63
13.6
CD200-BV421

Figure S8

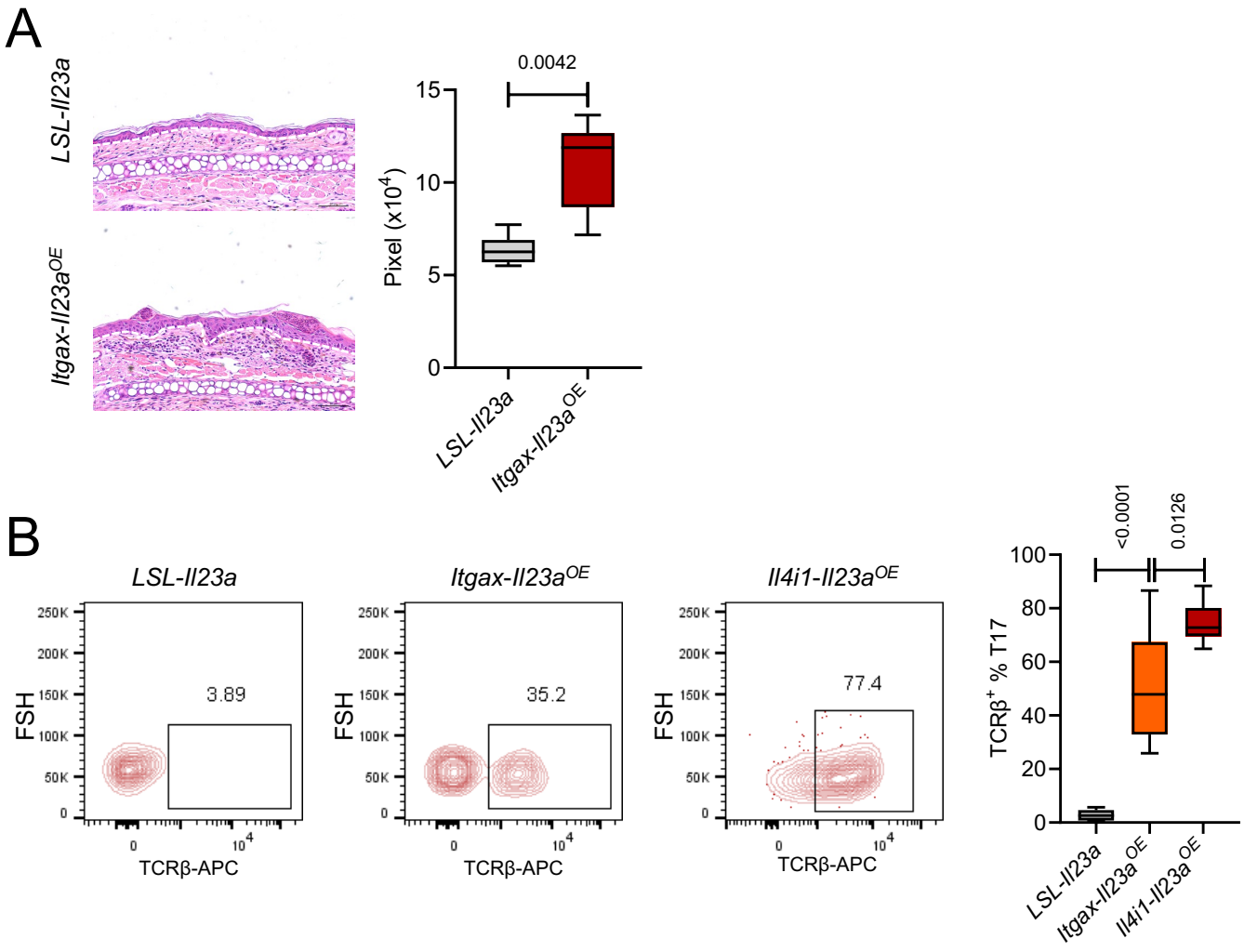
A
LSL-Il23a
Itgax-Il23a^OE
0.0042
Pixel (x10^4)
15
10
5
0
LSL-Il23a
Itgax-Il23a^OE
B
LSL-Il23a
Itgax-Il23a^OE
Il4i1-Il23a^OE
FSH
TCRβ-APC
3.89
35.2
77.4
250K
200K
150K
100K
50K
0
10^4
<0.0001
0.0126
TCRβ+ % T17
100
80
60
40
20
0
LSL-Il23a
Itgax-Il23a^OE
Il4i1-Il23a^OE

Figure S9

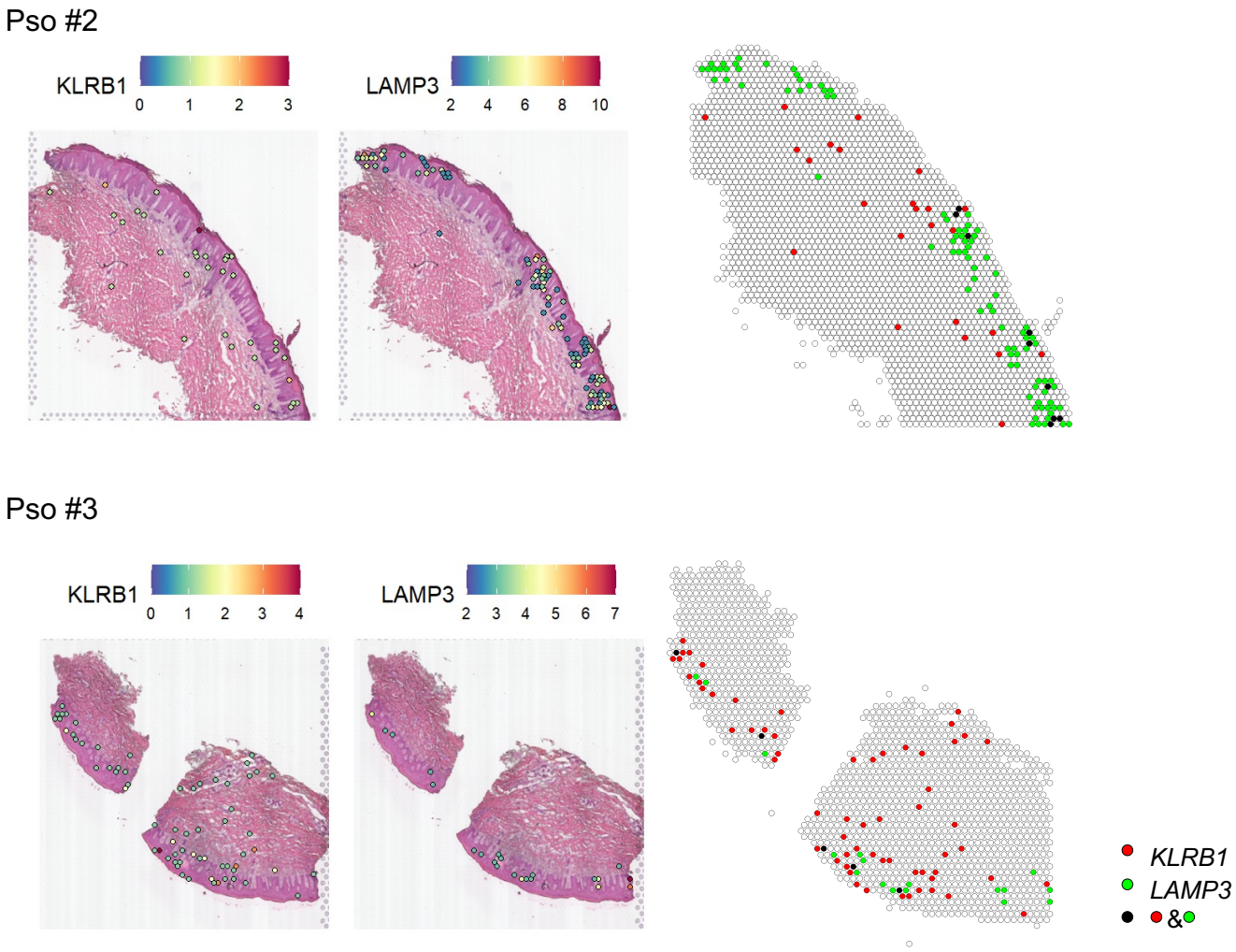
Pso #2
KLRB1
0 1 2 3
LAMP3
2 4 6 8 10
Pso #3
KLRB1
0 1 2 3 4
LAMP3
2 3 4 5 6 7
KLRB1
LAMP3
&